

Solar Sail Orbital Motion About Asteroids and Binary Asteroid Systems

Heiligers, Jeannette; Scheeres, Daniel J.

DOI

[10.2514/1.G003235](https://doi.org/10.2514/1.G003235)

Publication date

2018

Published in

Journal of Guidance, Control, and Dynamics: devoted to the technology of dynamics and control

Citation (APA)

Heiligers, J., & Scheeres, D. J. (2018). Solar Sail Orbital Motion About Asteroids and Binary Asteroid Systems. *Journal of Guidance, Control, and Dynamics: devoted to the technology of dynamics and control*, 41(9), 1947-1962. <https://doi.org/10.2514/1.G003235>

Important note

To cite this publication, please use the final published version (if applicable). Please check the document version above.

Copyright

Other than for strictly personal use, it is not permitted to download, forward or distribute the text or part of it, without the consent of the author(s) and/or copyright holder(s), unless the work is under an open content license such as Creative Commons.

Takedown policy

Please contact us and provide details if you believe this document breaches copyrights. We will remove access to the work immediately and investigate your claim.

Solar Sail Orbital Motion

About Asteroids and Binary Asteroid Systems

Jeannette Heiligers¹

Delft University of Technology, Delft, The Netherlands

and

Daniel J. Scheeres²

University of Colorado Boulder, Boulder, CO, USA

Solar radiation pressure (SRP) is a major orbital perturbation for missions to small bodies like asteroids and binary asteroid systems. This paper studies the utilization of SRP on a solar sail for asteroid mission applications, specifically to generate artificial equilibrium points (AEPs) and displaced periodic orbits in these systems. For the single asteroid case, contours of AEPs for constant sail acceleration magnitudes are found in the Hill + SRP problem as well as periodic orbits around these AEPs. The binary system is modeled by first adding a fourth-body perturbation to the Hill + SRP dynamics, demonstrating the effect of the smaller asteroid as an oscillatory motion superimposed on the unperturbed orbit. Truly periodic orbits are obtained in the bi-circular + SRP problem, showing the existence of so-called pole-sitter-like orbits above the binary system's orbital plane. Higher-fidelity dynamical effects are investigated for these pole-sitter-like orbits for binary system 1999 KW4, showing feasibility of the orbits around aphelion. All results are generated for near-term sail technology and for a simple, fixed sail attitude relative to the Sun. They therefore

¹ Marie Curie Research Fellow, Delft University of Technology, Faculty of Aerospace Engineering, Kluyverweg 1, 2629 HS Delft, the Netherlands and University of Colorado, Department of Aerospace Engineering Sciences, Colorado Center for Astrodynamics Research, Boulder, CO 80309, USA. M.J.Heiligers@tudelft.nl

² A. Richard Seebass Endowed Chair Professor, University of Colorado Boulder, Department of Aerospace Engineering Sciences, Colorado Center for Astrodynamics Research, Boulder, CO 80309, USA. Scheeres@colorado.edu

enable operable and unique vantage points from where to monitor the asteroid(s) over extended periods of time.

Nomenclature

A	=	Oblateness coefficient
\mathbf{a}_s	=	Solar sail acceleration vector, km/s^2 or dimensionless
a	=	Semi-major axis, km
a_0	=	Solar sail characteristic acceleration, km/s^2 or dimensionless
B	=	Non-Lambertian coefficient
e	=	Eccentricity
G	=	Universal gravity constant, $\text{km}^3/(\text{kg} \cdot \text{s}^2)$
i	=	Inclination, rad
$\hat{\mathbf{m}}$	=	Unit vector along the solar sail acceleration vector
m	=	Mass, kg
$\hat{\mathbf{n}}$	=	Unit vector normal to the solar sail
n	=	Mean motion of binary system's heliocentric orbit, rad/s
n_b	=	Mean motion of binary system, rad/s
P_{rot}	=	Rotational period of binary system, s
R	=	Body radius, km
\mathbf{r}	=	Solar sail position vector, km or dimensionless
\mathbf{r}_3	=	Position vector of perturbing body, km or dimensionless
\mathbf{r}_4	=	Position vector from solar sail to perturbing body, km or dimensionless
\tilde{r}	=	Reflectivity coefficient
$r _{a_0}$	=	Heliocentric distance at which a_0 is defined, km
r_H	=	Hill radius, km

$\hat{\mathbf{S}}$	=	Unit vector along the direction of sunlight
s	=	Fraction of photons that are specularly reflected
$\hat{\mathbf{t}}$	=	Unit vector tangential to the sail
t	=	Time, s or dimensionless
U	=	Effective potential, km^2/s^2 or dimensionless
U_{J_2}	=	Dimensionless perturbing potential due to oblateness
α	=	Cone angle, rad
ε	=	Emissivity coefficient
ξ	=	Continuation parameter
ϑ	=	Cone half-angle, rad
θ	=	True anomaly, rad
κ	=	Unit of distance, km
λ	=	Eigenvalue
μ	=	Mass ratio of the circular restricted three-body problem
$\tilde{\mu}$	=	Gravitational parameter, km^3/s^2
$\tilde{\mu}_3$	=	Gravitational parameter of perturbing body, km^3/s^2
ν	=	Ratio of main binary asteroid mass and total binary asteroid mass
ρ	=	Magnitude of position vector projected on the (x, y) -plane
$\mathbf{\Omega}$	=	Angular velocity vector of reference frame, rad/s or dimensionless
Ω_S	=	Dimensionless angular rate of Sun around the binary system
ω	=	Angular rate of binary system, rad/s

Subscripts

0	=	At the initial time
---	---	---------------------

1	=	Referring to, or with respect to, main binary asteroid
2	=	Referring to, or with respect to, smaller binary asteroid
3	=	Referring to perturbing body
b	=	Back of the sail
f	=	Front of the sail
max	=	Maximum value
n	=	Along the $\hat{\mathbf{n}}$ -vector
S	=	With respect to the direction of sunlight
t	=	Along the $\hat{\mathbf{t}}$ -vector
x, y, z	=	Along the $\hat{\mathbf{x}}, \hat{\mathbf{y}}, \hat{\mathbf{z}}$ -axis
$\hat{\square}$	=	Denotes unit vector
$\dot{\square}$	=	Denotes first order derivative with respect to time
$\ddot{\square}$	=	Denotes second order derivative with respect to time

I. Introduction

SOLAR sailing is a relatively new, but flight-proven form of low-thrust space propulsion [1, 2]. By exploiting the solar radiation pressure (SRP) on a large reflective membrane, solar sails can produce thrust without relying on an onboard supply of fuel [3, 4]. This unique capability allows solar sails to produce thrust over extended periods of time and build up large amounts of momentum over the mission lifetime. Solar sails are therefore particularly suited for long-duration and high-energy missions such as precessing an elliptical Earth-centered orbit to observe the Earth's magnetotail over extended periods of time [5-8], hovering sunward of the L_1 -point to increase the warning time for space weather events [9, 10], and finally, and of importance to the current paper, using the sail for close-up observations of a range of small bodies in a multiple near-Earth asteroid (NEA) rendezvous mission [11, 12]. The capabilities of solar sails for visiting NEAs will be demonstrated by NASA's proposed solar sail NEA Scout mission [13].

The NEA Scout mission, as well as other asteroid missions such as NASA’s ongoing OSIRIS-REx mission³, are only two of many examples that highlight the significant increase in the interest in small body missions over recent years. This interest originates from a scientific perspective, because small bodies hold key information to the understanding of the origin and evolution of our Solar System, but also from a planetary defense perspective as well as their potential as targets for future human space exploration activities. For close-up investigations of asteroids and other small bodies, a thorough understanding of the orbital motion around these bodies is key and abundant research in this field has demonstrated the challenge that solar radiation pressure poses to such small-body missions [14, 15]. However, instead of considering it an undesirable perturbation, we exploit SRP in this paper through the use of solar sails to create entirely new orbital opportunities in the vicinity of asteroids.

The dynamics of a solar sail in close proximity to an asteroid have not yet been investigated in great detail. Previous work has mainly focused on terminator orbits [16] and the existence of hovering points at an asteroid [16-20]. These hovering points originate when adding a solar sail (or any low-thrust propulsion system [21, 22]) to a three-body system: any three-body system exhibits the well-known Lagrange points which can be extended to three-dimensional surfaces of artificial equilibrium points through a correct selection of sail acceleration and attitude. The purpose of the current paper is to complement these initial investigations with the existence of solar sail periodic orbits about these AEPs as well as extending the analyses to binary asteroid systems. In a binary system, constant surfaces of artificial equilibrium points cannot be obtained because the system is time-dependent: the binary asteroids orbit each other while also orbiting the Sun. However, stationary solutions to the dynamics *at a particular time* can be used to generate a well-informed guess for solar sail periodic orbits high above the binary asteroid’s orbital plane, so-called pole-sitter-like orbits. The orbits developed in this paper, either above a single asteroid or a binary asteroid pair allow unique, geostationary-equivalent vantage points from where the asteroid or asteroid pair can be observed over extended periods of time.

For the analyses in this paper we will initially assume a spherical, point mass asteroid, a perfectly reflecting solar sail (“ideal” solar sail model), and a circular heliocentric orbit of the asteroid/binary system about the Sun. Furthermore, for the binary system, we will at first assume a zero inclination between the plane in which the two binary asteroids orbit each other and their heliocentric orbital plane. The effect of these assumptions will be

³ OSIRIS-Rex, NASA; data available online at <https://www.nasa.gov/osiris-rex> [retrieved June 2017]

demonstrated for the most promising and unstable orbits, i.e., the pole-sitter-like orbits, through a high-fidelity analysis, showing that the orbits still exist when considering the actual heliocentric orbit parameters and a more realistic solar sail reflectance model and shape of the binary asteroid pair. Finally, to greatly simplify mission operations, all orbits are generated for a simple solar sail steering law that assumes a fixed attitude of the sail with respect to the incoming sunlight. Such an attitude can, in theory, be achieved passively through a correct offset between the sailcraft's center-of-pressure and center-of-mass.

II. Dynamical Models

Depending on whether the solar sail motion about a single asteroid or a binary system is considered, either the framework of the Hill + SRP problem (single asteroid), the Hill four-body + SRP problem or the bi-circular + SRP problem (both binary system) is employed. Note that, for the single asteroid case, the Hill + SRP problem is required due to the very small mass of the asteroid with respect to the Sun and the expected close proximity of the spacecraft with respect to the asteroid [16].

The reference frames involved in all three dynamical systems are illustrated in Figure 1. When considering the Sun-asteroid Hill + SRP problem or the Hill four-body + SRP problem, a rotating reference frame $R_1(\hat{\mathbf{x}}, \hat{\mathbf{y}}, \hat{\mathbf{z}})$ is employed that is centered at the (main) asteroid with the x -axis along the Sun-asteroid line, the z -axis perpendicular to the asteroid's heliocentric orbital plane and the y -axis completing the right-handed reference frame. When considering the binary asteroid bi-circular + SRP problem, again a rotating reference frame $R_2(\hat{\mathbf{x}}, \hat{\mathbf{y}}, \hat{\mathbf{z}})$ is employed, now with the x -axis connecting the two asteroids of the binary system, the z -axis perpendicular to the binary system's orbital plane and the y -axis completing the right-handed reference frame. The solar sail dynamics in either model is given by [3, 16]:

$$\ddot{\mathbf{r}} + 2\boldsymbol{\Omega} \times \dot{\mathbf{r}} = \nabla U + \mathbf{a}_s, \quad (1)$$

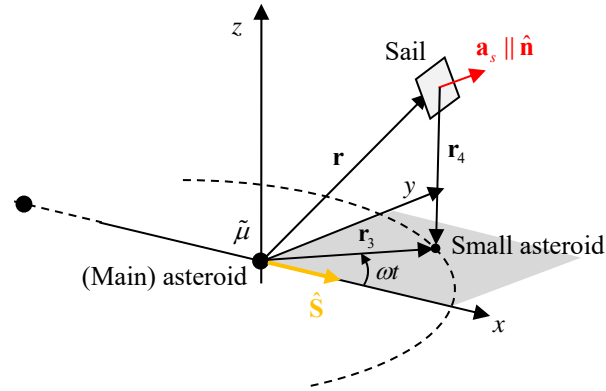
In Eq. (1), \mathbf{r} is the solar sail position vector in either $R_1(\hat{\mathbf{x}}, \hat{\mathbf{y}}, \hat{\mathbf{z}})$ or $R_2(\hat{\mathbf{x}}, \hat{\mathbf{y}}, \hat{\mathbf{z}})$, $\boldsymbol{\Omega} = \Omega \hat{\mathbf{z}}$ with Ω either the asteroid's orbit angular velocity around the Sun (Hill (four-body) + SRP problem) or the dimensionless angular velocity of the two asteroids around their common center-of-mass (bi-circular + SRP problem), U is the effective potential and \mathbf{a}_s is the solar sail acceleration vector. Note that in the case of the bi-circular + SRP problem a set of canonical units is used whereby the sum of the two asteroid masses, the distance between them (κ) and $P_{rot} / 2\pi$

are taken as the unit of mass, length, and time, respectively, where P_{rot} is the rotational period of the binary system.

The definition of the effective potential is different for the three dynamical systems and is given by [3, 14, 16]:

$$U = \begin{cases} \frac{\tilde{\mu}}{r} - \frac{1}{2}\Omega^2(z^2 - 3x^2) & \text{Hill problem} \\ \frac{\tilde{\mu}}{r} - \frac{1}{2}\Omega^2(z^2 - 3x^2) + \tilde{\mu}_3\left(\frac{1}{r_4} - \frac{\mathbf{r}\cdot\mathbf{r}_3}{r_3^3}\right) & \text{Hill four-body problem} \\ \left(\frac{1-\mu}{r_1} + \frac{\mu}{r_2}\right) + \frac{1}{2}(x^2 + y^2) + \mu_3\left(\frac{1}{r_4} - \frac{\mathbf{r}\cdot\mathbf{r}_3}{r_3^3}\right) & \text{Bi-circular problem} \end{cases} \quad (2)$$

a)



b)

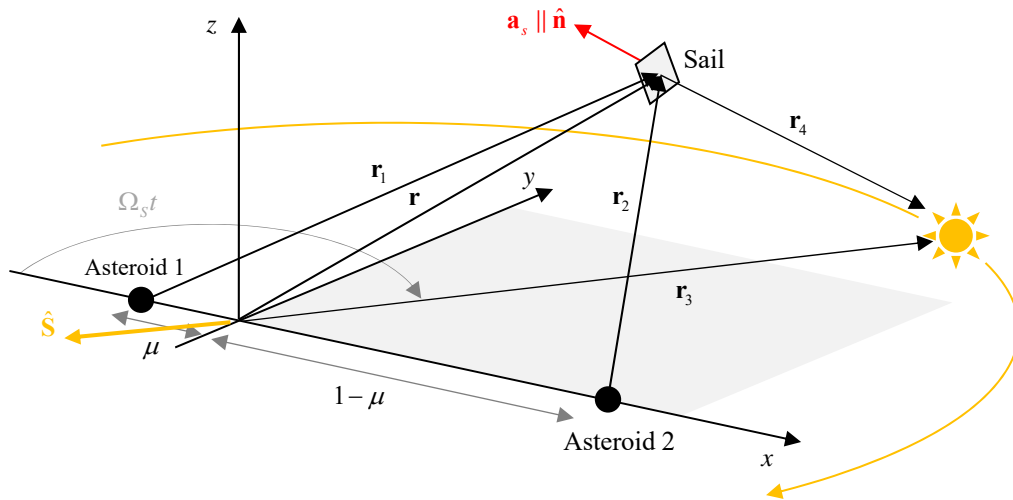


Figure 1 Schematics of reference frames. a) Hill (four-body) + SRP problem. b) Bi-circular + SRP problem.

with $\tilde{\mu}$ the gravitational parameter of the single/main asteroid, $\tilde{\mu}_3$ the gravitational parameter of the perturbing, smaller asteroid in the binary system, $\mu = m_2 / (m_1 + m_2)$ (with m_1 and m_2 the masses of ‘Asteroid 1’ and ‘Asteroid 2’, respectively), $\mu_3 = m_3 / (m_1 + m_2)$ (with m_3 the mass of the Sun) and r_1 , r_2 , r_3 and r_4 the magnitude of the vectors $\mathbf{r}_1 = \mathbf{r} + [\mu \ 0 \ 0]^T$, $\mathbf{r}_2 = \mathbf{r} + [\mu - 1 \ 0 \ 0]^T$, \mathbf{r}_3 the (dimensionless) position vector of the perturbing body, and $\mathbf{r}_4 = \mathbf{r}_3 - \mathbf{r}$, see Figure 1. The vector \mathbf{r}_3 in either the Hill four-body or the bi-circular problem is defined as:

$$\mathbf{r}_3 = \begin{cases} r_3 [\cos \omega t & \sin \omega t & 0]^T & \text{Hill four-body problem} \\ -r_3 \hat{\mathbf{S}} & & & \text{Bi-circular problem} \end{cases}. \quad (3)$$

Let’s first consider the parameters involved in the first line of Eq. (3), for the Hill four-body problem: r_3 equals the distance between the binary asteroids and ω is the angular rate of the binary system in $R_2(\hat{\mathbf{x}}, \hat{\mathbf{y}}, \hat{\mathbf{z}})$ (note that this is different from the binary system’s mean motion):

$$\omega = n_b - n \quad (4)$$

where n and n_b are the mean motions of the binary system’s heliocentric orbit and the binary system, respectively.

Let’s now consider the parameters involved in the second line of Eq. (3), for the bi-circular problem: r_3 equals the dimensionless Sun-sail distance and $\hat{\mathbf{S}}$ is the direction of sunlight (see Figure 1b). Using the definitions in Figure 1, the unit vector $\hat{\mathbf{S}}$ can be defined as:

$$\hat{\mathbf{S}} = \begin{cases} [1 \ 0 \ 0]^T & \text{Hill (four-body) + SRP problem} \\ [\cos(\Omega_s t) \ -\sin(\Omega_s t) \ 0]^T & \text{Bi-circular + SRP problem} \end{cases} \quad (5)$$

with Ω_s the dimensionless angular rate of the Sun around the binary system, defined as:

$$\Omega_s = \frac{1}{n_b} (n_b - n) \quad (6)$$

The dimensionless period of the Sun around the binary system (hereafter referred to as the Sun’s synodic period) can then be expressed as $2\pi / \Omega_s$. Finally, the solar sail acceleration vector $\mathbf{a}_s = [a_{s,x} \ a_{s,y} \ a_{s,z}]^T$ for an ideal solar sail, can be defined as:

$$\mathbf{a}_s = a_0 (\hat{\mathbf{S}} \cdot \hat{\mathbf{n}})^2 \hat{\mathbf{n}} \quad (7)$$

with $\hat{\mathbf{n}}$ the unit vector normal to the sail membrane and a_0 the solar sail characteristic acceleration *at the asteroid's or binary system's heliocentric distance* (dimensionless for the case of the bi-circular + SRP problem). The characteristic acceleration is the acceleration produced by the sail when oriented perpendicular to the incoming sunlight, i.e., $\hat{\mathbf{n}} = \hat{\mathbf{S}}$. The second column of Table 2 lists the characteristic accelerations at 1 AU for a range of previous and proposed solar sail missions. Because the expected asteroid-sail distances are small compared to the Sun-asteroid distance, Eq. (7) assumes a constant SRP (both in magnitude and direction) throughout the (binary) asteroid system. The produced solar sail acceleration thus does not depend on the location of the solar sail in $R_1(\hat{\mathbf{x}}, \hat{\mathbf{y}}, \hat{\mathbf{z}})$ or $R_2(\hat{\mathbf{x}}, \hat{\mathbf{y}}, \hat{\mathbf{z}})$. Equation (7) also takes into account the reduction in sail acceleration when pitching the normal to the sail away from the direction of sunlight through the term $(\hat{\mathbf{S}} \cdot \hat{\mathbf{n}})^2$. Finally, while the Sun is stationary in the Hill (four-body) + SRP problem, the Sun orbits around the binary system in the bi-circular + SRP problem and the smaller asteroid orbits around the main asteroid in the Hill four-body + SRP problem. In those cases, the vectors \mathbf{r}_3 and $\hat{\mathbf{S}}$ change over time, which introduces a time dependency into the dynamics, causing the last two systems of equations in Eq. (1) to be non-autonomous.

III. Artificial Equilibrium Points

When considering the Hill + SRP problem, the approach in Reference [3] can be adopted to find artificial equilibrium points (AEPs) at a single asteroid. When setting $\ddot{\mathbf{r}} = \dot{\mathbf{r}} = \mathbf{0}$ in Eq. (1), it becomes clear that, to create AEPs, the solar sail acceleration vector needs to counteract the gradient of the effective potential:

$$\nabla U = -\mathbf{a}_s. \quad (8)$$

The required direction of the sail acceleration can then be obtained by taking the cross product of both sides of Eq. (8) with $\hat{\mathbf{n}}$, resulting in

$$\nabla U \times \hat{\mathbf{n}} = \mathbf{0}, \quad (9)$$

which gives

$$\hat{\mathbf{n}} = -\frac{\nabla U}{|\nabla U|}. \quad (10)$$

Furthermore, the characteristic sail acceleration required to maintain a particular AEP can be obtained by taking the scalar product of Eq. (8) with $\hat{\mathbf{n}}$:

$$a_0 = -\frac{\nabla U \cdot \hat{\mathbf{n}}}{(\hat{\mathbf{S}} \cdot \hat{\mathbf{n}})^2} . \quad (11)$$

The results in terms of solar sail acceleration contours required to transform a particular location in the (x, z) - or (x, y) -plane of the Hill frame into an AEP appear in Figure 2, which are in agreement with the results found in Reference [16]. Note that the distances on the horizontal and vertical axes are made dimensionless with respect to the Hill radius, $r_H = \sqrt[3]{\tilde{\mu}/(3\Omega^2)}$, whereas the sail acceleration is made dimensionless with respect to the asteroid's gravitational acceleration at the Hill radius, $\tilde{\mu}/r_H^2$. Then, the figure can be applied to any asteroid at any heliocentric orbit radius. For example, the figure can be applied to asteroid Vesta, where details on the Hill radius and the actual required performance required from the solar sail can be found in Table 1 and Table 2, respectively. For example, at Vesta and for a Sunjammer-type solar sail, the normalized characteristic acceleration a_0 is

computed as: $a_0 = \frac{0.2153 \times 10^{-6} \left(\frac{AU}{a}\right)^2}{\tilde{\mu}/r_H^2} = 36.715$. The light-blue contours in Figure 2 ($a_0 = 30$) can thus be

achieved with a solar sail similar to the technology proposed for Sunjammer. Finally, note that AEPs do not exist in the regions indicated with 'infeasible region' as they would require a solar sail acceleration component in the direction of the Sun, which the sail is unable to generate [3]. The transition from 'feasible' to 'infeasible' is provided through the thick black lines.

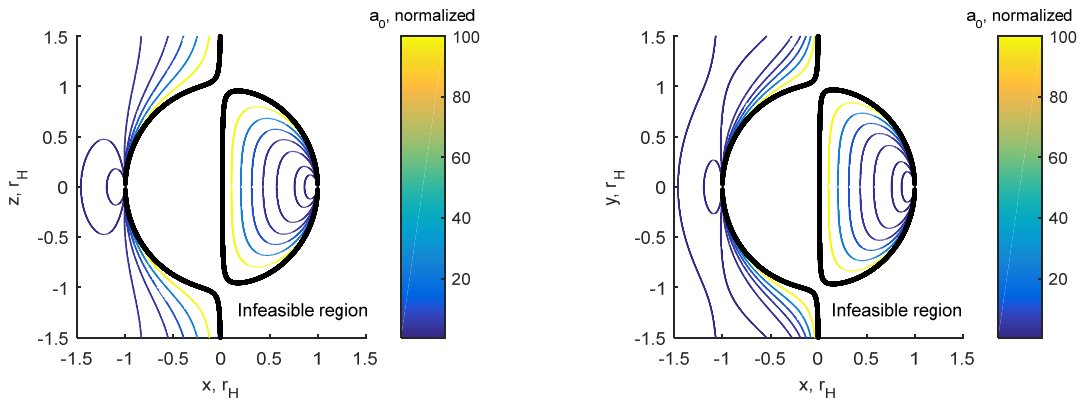


Figure 2 Solar sail acceleration contours to maintain AEPs in the Hill + SRP problem.

Table 1 Asteroid Vesta parameters (with assumptions).

Parameter	Value
Gravitational parameter, $\tilde{\mu}$	14.2568
Semi-major axis, a	2.36 AU
Eccentricity	0.08874 \rightarrow assumed to be 0
Hill radius, r_H	116,365 km
Gravitational acceleration at Hill radius	$1.0529 \times 10^{-3} \text{ mm/s}^2$

**Table 2 Characteristic accelerations of previous and proposed solar sail missions.
Dimensional values at 1 AU and normalized values.**

Mission	Characteristic acceleration at 1 AU, mm/s^2	Hill normalization		Bi-circular normalization		
		Vesta	"Condensed 1999 KW4"	1999 KW4		
				At perihelion	At 1 AU	At aphelion
IKAROS [1]	0.0059	1.006	444.84	5.792	0.2324	0.1979
NanoSail-D2 [2]	0.0178	3.035	1,342.06	17.476	0.7012	0.5970
LightSail-1 [23]	0.0652	11.118	4,915.86	64.013	2.5683	2.1869
NEA Scout [13]	0.0593	10.112	4,471.02	58.221	2.3359	1.9890
Sunjammer [10]	0.2153	36.715	16,232.89	211.380	8.4810	7.2215

When applying the same approach to the bi-circular problem, the time dependency in the dynamics (through the vectors \mathbf{r}_3 and $\hat{\mathbf{S}}$) prevents us from finding constant surfaces of AEPs, i.e., AEPs that can be maintained over time with a constant sail attitude and sail characteristic acceleration. This will be illustrated for a particular binary system, 1999 KW4, which has served as a test case in previous studies [24] and has well-documented characteristic [25, 26], see Table 3.

When setting $\ddot{\mathbf{r}} = \dot{\mathbf{r}} = \mathbf{0}$ for a specific time t in Eq. (1), the solar sail dimensionless characteristic acceleration contours of Figure 3 are obtained. Subplot a) holds at time $t = 0$, whereas subplot b) holds at $t = 0.25\pi / \Omega_S$, where the latter equals one eighth of the Sun's synodic period. Because the contours in Figure 3 are plotted for the

characteristic solar sail acceleration *at the binary asteroid's heliocentric distance*, the figure holds at any Sun-binary distance. Again, as an example, looking at the conditions at perihelion and for a Sunjammer-type sail, the resulting

normalized characteristic acceleration a_0 can be computed as:
$$a_0 = \frac{0.2153 \times 10^{-6} \left(\frac{AU}{a(1-e)} \right)^2}{\kappa / [P_{rot} / 2\pi]^2} = 211.380$$
. Note

that the actual Sun-binary distance (which in reality varies significantly as the binary 1999 KW4 is on a highly elliptic orbit) will affect the required dimensional solar sail performance to maintain a particular AEP as well as the angular rate of the Sun around the binary system, Ω_s (see Table 3).

Table 3 Binary system 1999 KW4 parameters [24-26] (with assumptions).

Parameter	Value
Binary system	
Total mass of system	$m_1 + m_2 = 2.472 \times 10^{12}$ kg
Ratio of primary body and total mass	$\nu = 0.9457$
Mass ratio	$\mu = m_2 / (m_1 + m_2) = 1 - \nu = 0.0543$
Distance between bodies	$\kappa = 2.54$ km
Average equatorial body radii (asteroid 1, asteroid 2)	$R_1 = 0.757$ km, $R_2 = 0.259$ km
Average polar body radii (asteroid 1, asteroid 2)	$R_{1,p} = 0.674$ km, $R_{2,p} = 0.175$ km
Rotational period of system	$P_{rot} = 17.458$ hr
Mean motion	$n_b = 9.9973 \times 10^{-5}$ rad/s
Rotation rate in $R_1(\hat{x}, \hat{y}, \hat{z})$	$\omega = 9.9774 \times 10^{-5}$ rad/s ($a = 1$ AU; $e = 0$)
Heliocentric orbit	
Semi-major axis	$a = 0.642$ AU \rightarrow assumed to be 1 AU
Eccentricity	$e = 0.688 \rightarrow$ assumed to be 0
Inclination	$i = 38.884$ deg \rightarrow assumed to be 0 deg
Mean motion	$n = 1.9911 \times 10^{-7}$ rad/s ($a = 1$ AU) $n = 3.8707 \times 10^{-7}$ rad/s ($a = 0.642$ AU)
Dimensionless angular rate of Sun in $R_2(\hat{x}, \hat{y}, \hat{z})$	$\Omega_s = 0.9980$ ($a = 1$ AU; $e = 0$) $\Omega_s = 0.9711$ (at perihelion) $\Omega_s = 0.9990$ (at aphelion)

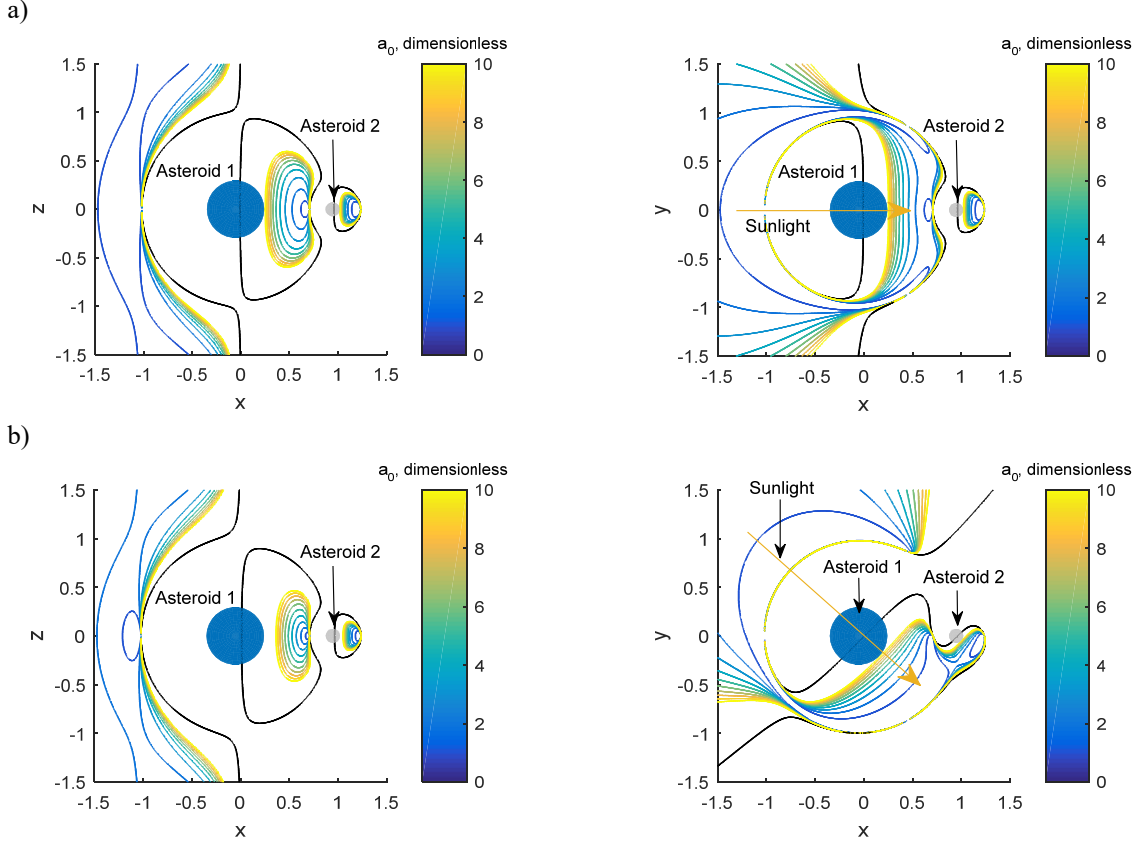


Figure 3 Dimensionless solar sail characteristic acceleration contours to maintain an AEP in the bi-circular + SRP problem of binary system 1999 KW4. a) At time $t = 0$. b) At time $t = 0.25\pi/\Omega_s$.

From comparing Figure 3a and Figure 3b it becomes clear that, as previously discussed, the required characteristic acceleration (as well as sail attitude) to maintain an AEP change over time. However, when plotting the contours on a plane perpendicular to the (x, y) -plane that co-rotates with the Sun, see the gray (ρ, z) -plane in Figure 4a, the location of some of the contours remains nearly fixed. This is demonstrated in Figure 4b that shows how the contours for $a_0 = 10$ evolve over time when projected onto the (ρ, z) -plane of Figure 4a. The color scale indicates the time, $t \in [0, 2\pi/\Omega_s]$, but only the colors of the second half of the Sun's synodic period are visible as contours overlap due to the symmetry of the problem. These insights will be used later in the paper to explore the existence of periodic orbits high above the binary system's orbital plane.

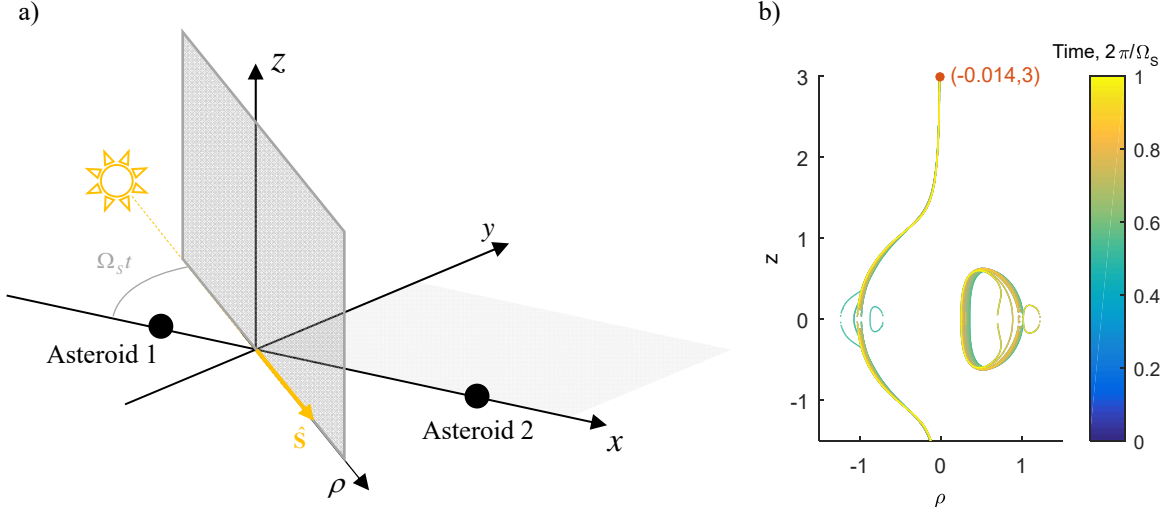


Figure 4 a) Schematic of (ρ, z) -plane co-rotating with the Sun. b) Time-evolution of AEP contours at 1999 KW4 for $a_0 = 10$ projected on the (ρ, z) -plane of subplot a).

IV. Solar Sail Periodic Orbits in the Hill + SRP Problem

Rather than hovering at a specific AEP, the solar sail can also be inserted into a periodic orbit around the AEP. The existence of such periodic orbits and the techniques required to obtain these periodic orbits have already been proven in the Sun-Earth circular restricted three-body problem [27, 28]. Adapting the technique to the dynamics of the Hill + SRP problem, an initial guess for such solar sail periodic orbits can be obtained through the following approach (with details in Reference [28]): first, we fix the attitude of the sail to the one of the AEP, see Eq. (10); we then approximate the equations of motion of the Hill + SRP dynamics in the neighborhood of the AEP by linearization, but we expand the effective potential and solar sail acceleration terms to third order with a Taylor series; finally, we use the Lindstedt-Poincaré method to find the third-order solution to this approximated dynamical system.

Because the resulting solar sail periodic orbits are only approximations to the solutions of the full non-linear system, the orbit quickly diverges when integrating these initial conditions in Eq. (1). A differential correction scheme [10, 28, 29] is therefore employed to correct the initial conditions and find true solar sail periodic orbits in the full non-linear system.

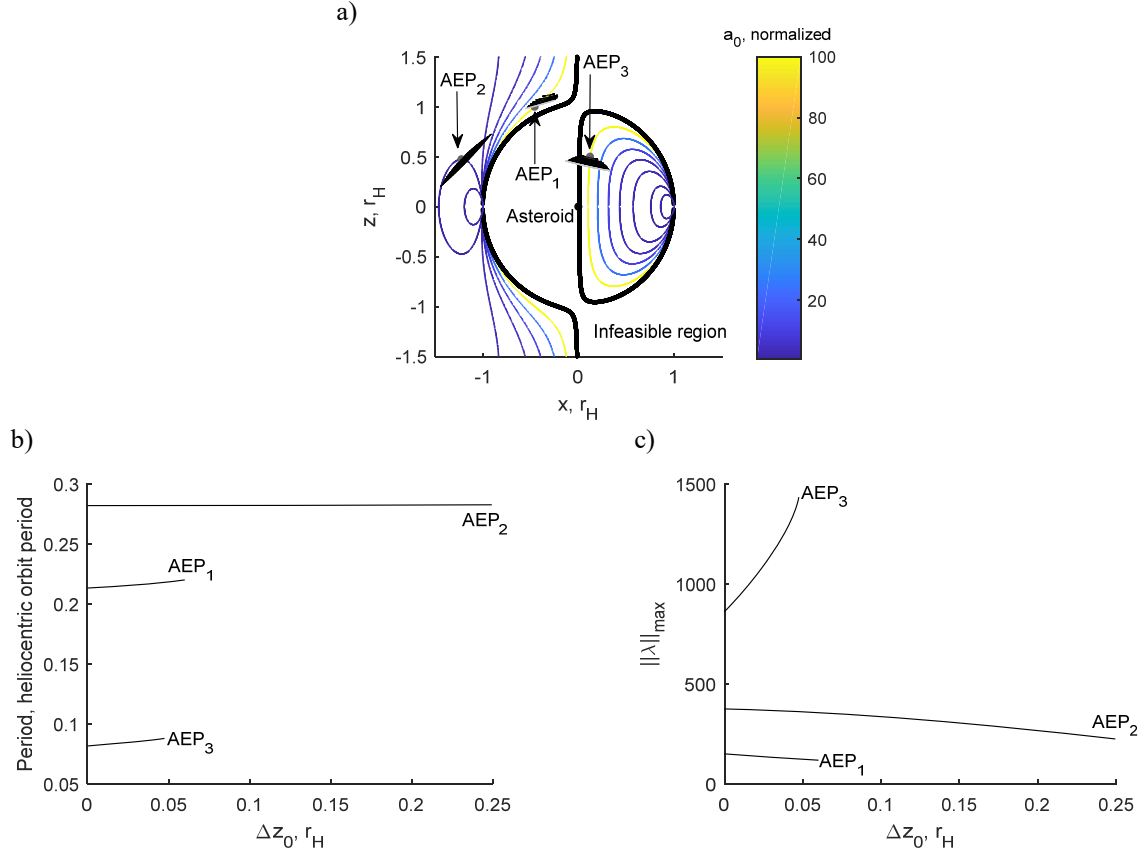


Figure 5 a) Families of solar sail periodic orbits around three AEPs in the Hill + SRP problem. b) Period as a fraction of the asteroid’s heliocentric orbital period. c) Linear stability.

Families of such periodic orbits around randomly selected AEPs appear in Figure 5a. Note that two families of periodic orbits emanate from each AEP, one for each of the two pairs of the complex conjugate eigenvalues of the linearized system, but that for conciseness only one such family appears in Figure 5a. The grey orbit indicates the third-order approximation of the orbit while the black orbits are families of orbits that exist in the full non-linear system. These families are constructed through a continuation on the initial z -coordinate, z_0 , with a step size of $5 \times 10^{-4} r_H$ (with r_H the Hill radius). The family is truncated at a maximum total increase in z_0 , Δz_0 , of $0.25 r_H$ or when the differential correction scheme does not converge for the given step size. Note that all orbits exist for a constant sail attitude with respect to the direction of sunlight, prescribed by the required attitude of the AEP, see Eq. (10). The periods of the orbits in Figure 5a are provided in Figure 5b, showing that the period is a significant fraction of the heliocentric orbital period of the asteroid about the Sun. Furthermore, Figure 5c provides the linear

stability of the orbits through the norm of the largest eigenvalue, $\|\lambda\|_{\max}$, of the monodromy matrix (the state transition matrix evaluated after one full orbit). If the norm of all six eigenvalues lie on the unit circle, i.e., $\|\lambda\|_{\max} = 1$, the orbit is considered stable. For norm values larger than one, the orbit is considered unstable. From Figure 5c it is clear that all orbits are unstable, but with increasing stability for AEPs 1 and 2 for increasing z -amplitudes, while the opposite holds true for AEP 3. Finally, while Figure 5 holds for any asteroid, Figure 6 provides specific details for the orbits at asteroid Vesta.

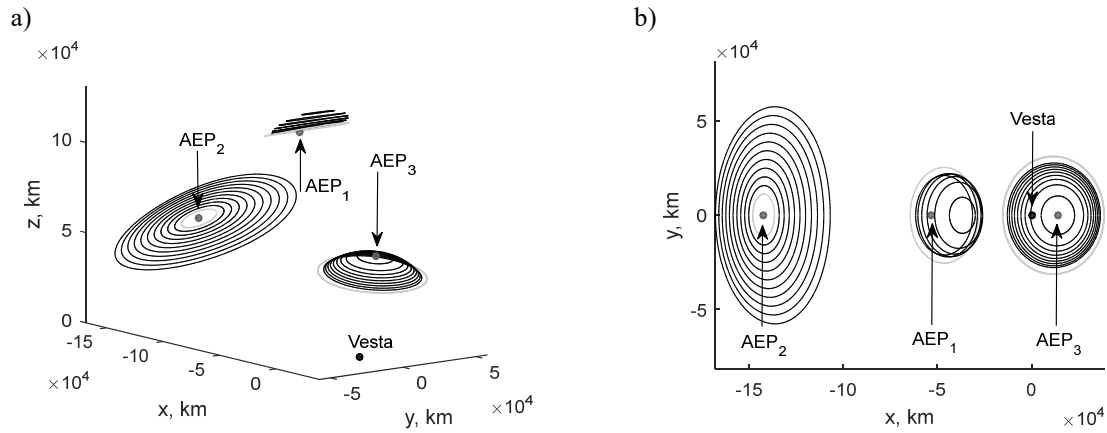


Figure 6 Families of solar sail periodic orbits around three AEPs at asteroid Vesta. a) 3D view. b) (x,y)-projection.

V. Solar Sail Periodic Orbits in the Hill Four-Body + SRP Problem

The time dependency in the dynamics of the binary system, and therefore in the surfaces of AEPs, again prevents us from applying the approach in the previous section to the bi-circular + SRP problem. However, the Hill four-body + SRP problem provides a suitable alternative framework to account for the perturbation from the smaller asteroid. Because the period of the solar sail orbits (see Figure 5b) and the period of the smaller asteroid around the main asteroid (P_{rot} , see Table 3) are not commensurable, periodic orbits will no longer exist. However, by using techniques such as multiple shooting differential correction, trajectories may still be found that remain close to the periodic orbit. To that end, the following approach is adopted: at first, the total mass of the binary system is assumed to be condensed into a single asteroid, reducing the problem to the Hill + SRP problem for which the same solar sail periodic orbits exist as shown in Figure 5a with their periods and stability indicated in Figure 5b and c. In actual

dimensions, the size and location of the periodic orbits will depend on where the binary system is in its heliocentric orbit. For now, assuming the binary to be on a circular 1 AU heliocentric orbit, the results in Figure 7 are obtained. Note that, under conditions similar to those at perihelion, the orbits will exist closer to the asteroid and under conditions similar to those at aphelion, they will exist farther away from the asteroid. However, as the solar sail orbital period is a significant fraction of the binary asteroid's heliocentric orbit period (see again Figure 5b), conditions will actually change along the orbit.

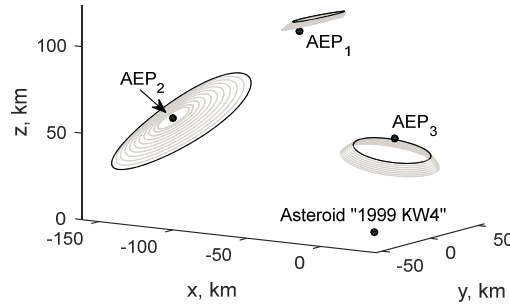


Figure 7 Families of solar sail periodic orbits around three AEPs at an asteroid with mass equal to binary system 1999 KW4 on a circular 1 AU heliocentric orbit.

Subsequently, a continuation is started to gradually distribute the total mass over the two asteroids, while at the same time gradually separating the two asteroids up to the total separation distance, $\kappa = 2.54$ km (see Table 3). Denoting the continuation parameter as $0 < \xi \leq (1 - \nu)$, with $\nu = 0.9457$ the ratio of the main asteroid mass and the total system mass (see Table 3), the mass distribution during the continuation can be expressed as:

$$\begin{aligned} \tilde{\mu} &= (1 - \xi)G(m_1 + m_2) \\ \tilde{\mu}_3 &= \xi G(m_1 + m_2) \end{aligned} \quad (12)$$

with G the universal gravity constant. At each step of the continuation, a multiple shooting differential correction (MSDC) scheme is employed to find the trajectory that remains in close proximity of the periodic orbits in Figure 7. MSDC divides an initial guess of the trajectory into segments by defining patch points at appropriate locations. Subsequently, two differential correction ‘levels’ are applied to sequentially adjust the position of the patch points and the velocities at the patch points to find a trajectory that holds under the dynamics of the Hill four-body + SRP problem. Here, an accuracy on the mismatch in position at each patch point of 10^{-9} km is used and a mismatch in velocity of 10^{-9} km/s, *summed* over all patch points, is allowed. Note that such small accuracies are required to ensure that a reintegration of the trajectory from the very first to the very last patch point does not lead to

divergence. As initial guess for the very first step in the continuation (i.e., for a very small value for ξ), the black periodic orbits in Figure 7 are used, i.e., the orbits with the largest out-of-plane amplitude. The result obtained from this first step in the continuation is then used as initial guess to solve for a slightly larger value for ξ and this process is repeated until $\xi = (1 - \nu)$. Further details on the MSDC scheme and its implementation can be found in References [30-32].

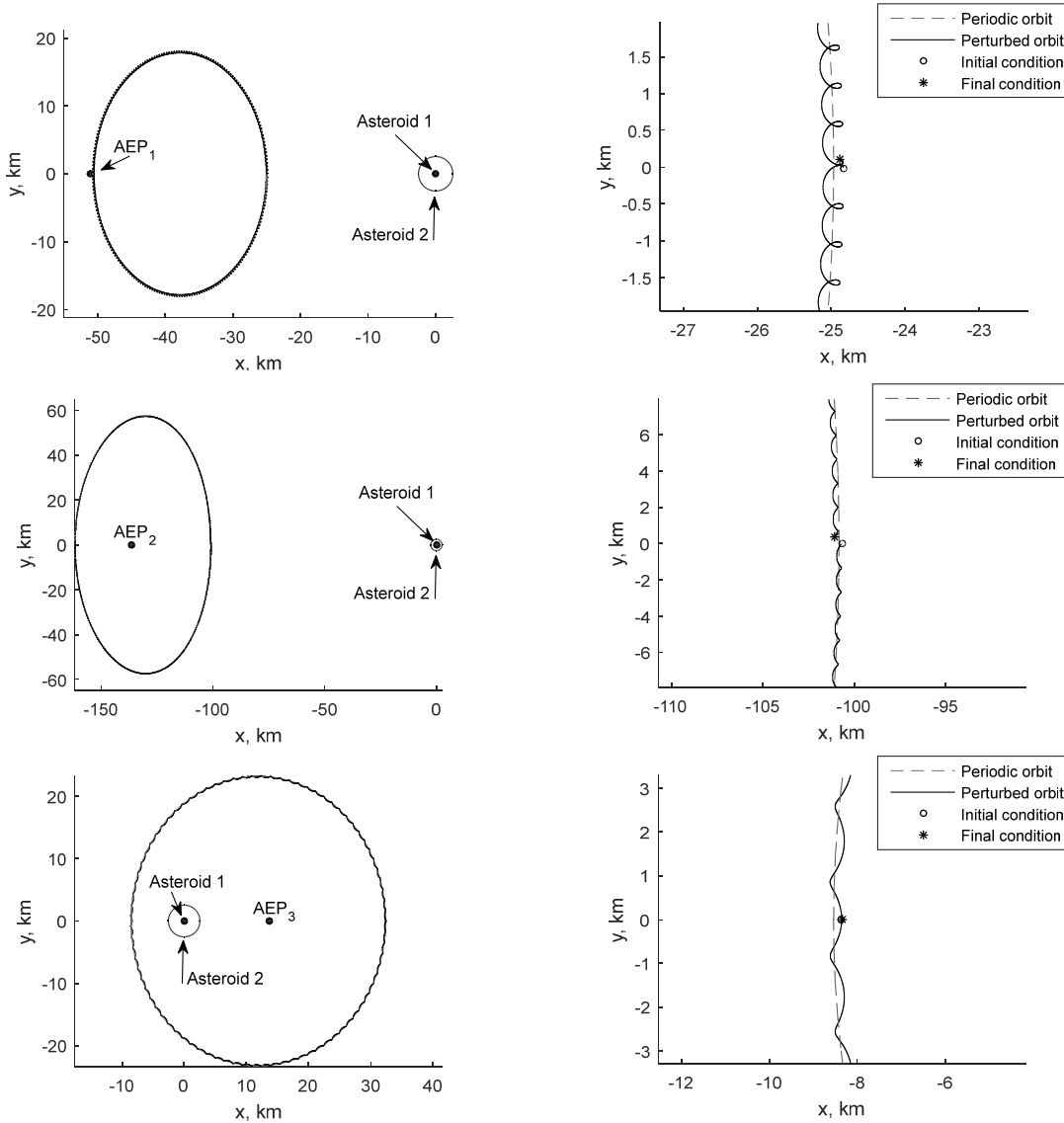


Figure 8 Effect of smaller binary asteroid on the black periodic orbits in Figure 7 modelled in the 1999 KW4 Hill four-body + SRP dynamics. The right column provides details of the figures on the left.

The result of the MSDC scheme is provided in Figure 8, which shows the original periodic orbit in the Hill + SRP problem (using a dashed grey line) and the perturbed orbits in the Hill four-body + SRP problem (in black). Here, the effect is evaluated for the duration of a single revolution of the original, periodic orbit. The black lines clearly show the effect of the binary system's smaller asteroid as a short-duration oscillatory motion around the periodic orbits of the Hill + SRP problem. Again note that these results hold under the assumption that the binary asteroid is on a circular 1 AU heliocentric orbit. As mentioned above, under conditions similar to those at perihelion, the orbits exist closer to the asteroid and therefore the perturbing effect of the smaller asteroid will be more significant and vice versa at aphelion.

VI. Solar Sail Pole-sitter-like Orbits in the Bi-circular + SRP Problem

Considering the smaller asteroid in the binary system as a perturbing body, as in the previous section, results in the non-periodic motion shown in Figure 8. This section aims at finding true periodic orbits above the binary system. In particular, so-called pole-sitter-like orbits will be investigated.

An initial guess for these pole-sitter-like orbits can be obtained from the information provided in Figure 4 as well as the techniques previously developed to obtain pole-sitter orbits at Earth [33, 34] and other inner-Solar System planets [35]. The approach consists of assuming a particular shape for the orbit, inverting the equations of motion to obtain the required solar sail acceleration vector and using the resulting initial condition as an initial guess in a differential corrector scheme.

The assumed orbit is schematically shown in Figure 9. The orbit lies on a cone with half-angle \mathcal{G} around the z -axis, maintains a constant distance from the binary system's orbital plane and has an orbital period equal to the Sun's synodic period of $2\pi/\Omega_S$. As such, the position, velocity and acceleration in the orbit can be expressed as:

$$\mathbf{r} = \begin{bmatrix} x \\ y \\ z \end{bmatrix} = \begin{bmatrix} r \sin \mathcal{G} \cos \Omega_S t \\ -r \sin \mathcal{G} \sin \Omega_S t \\ r \cos \mathcal{G} \end{bmatrix}, \quad \dot{\mathbf{r}} = \begin{bmatrix} \dot{x} \\ \dot{y} \\ \dot{z} \end{bmatrix} = \begin{bmatrix} -\Omega_S r \sin \mathcal{G} \sin \Omega_S t \\ -\Omega_S r \sin \mathcal{G} \cos \Omega_S t \\ 0 \end{bmatrix}, \quad \ddot{\mathbf{r}} = \begin{bmatrix} \ddot{x} \\ \ddot{y} \\ \ddot{z} \end{bmatrix} = \begin{bmatrix} -\Omega_S^2 r \sin \mathcal{G} \cos \Omega_S t \\ \Omega_S^2 r \sin \mathcal{G} \sin \Omega_S t \\ 0 \end{bmatrix}. \quad (13)$$

The initial condition (subscript '0') can then easily be obtained by substituting $t=0$ in Eq. (13). Finally, as a guess for r and \mathcal{G} , the results for the AEP indicated with a round marker in Figure 4b are used:

$$\begin{aligned} r &= \sqrt{\rho^2 + z^2} = \sqrt{0.014^2 + 3^2} \\ \mathcal{G} &= \tan^{-1}(\rho/z) = \tan^{-1}(0.014/3). \\ a_0 &= 10 \end{aligned} \quad (14)$$

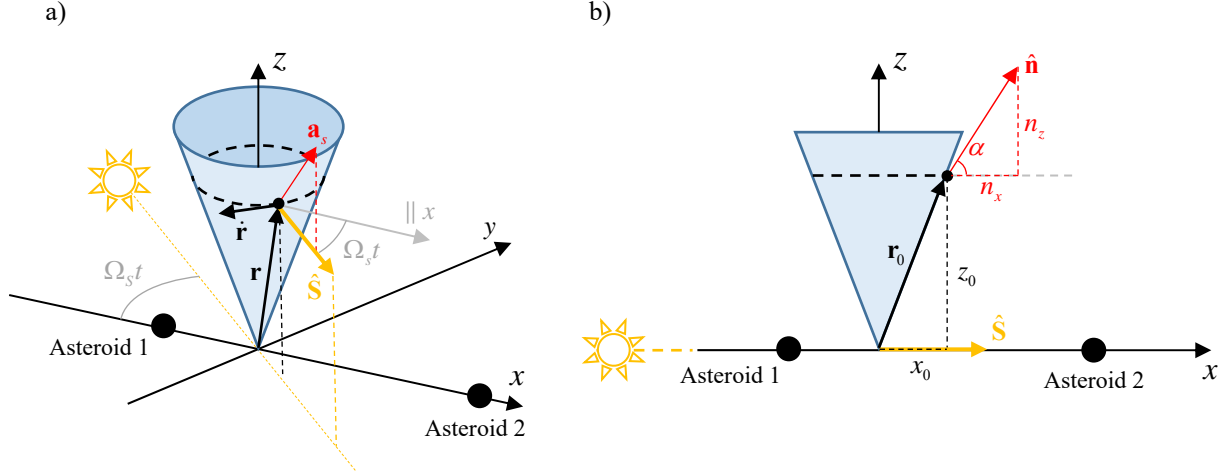


Figure 9 Schematic of assumed pole-sitter-like orbit. a) Generic case. b) Initial condition.

With the evolution of the states preassigned, the equations of motion in Eq. (1) can be inverted to find a guess for the required solar sail normal vector at the initial time:

$$\begin{aligned}
 n_{x,0} &= \sqrt[3]{\frac{1}{a_0} \left(\ddot{x}_0 - 2\dot{y}_0 - x_0 + \frac{1-\mu}{r_{1|0}^3} (\mu + x_0) + \frac{\mu}{r_{2|0}^3} (-(1-\mu-x_0)) - \mu_3 \left(\frac{1}{r_3^2} - \frac{x_0 + r_3}{r_{4|0}^3} \right) \right)} \\
 n_{y,0} &= 0 \\
 n_{z,0} &= \frac{z_0}{a_0 n_x^2} \left(\frac{1-\mu}{r_{1|0}^3} + \frac{\mu}{r_{2|0}^3} + \frac{\mu_4}{r_{4|0}^3} \right)
 \end{aligned} \tag{15}$$

$$\hat{\mathbf{n}}_0 = \frac{\begin{bmatrix} n_{x,0} & 0 & n_{z,0} \end{bmatrix}^T}{\left\| \begin{bmatrix} n_{x,0} & 0 & n_{z,0} \end{bmatrix}^T \right\|}. \tag{16}$$

Finally, we assume that the attitude of the sail *with respect to the Sun co-rotating frame* of Figure 4a, $\hat{\mathbf{n}}_s$, *remains constant over time*. Because at time $t=0$ the equality $\hat{\mathbf{n}}_s = \hat{\mathbf{n}}_0$ holds, the normal vector in the $R_2(\hat{x}, \hat{y}, \hat{z})$ -frame (see Figure 1b) at any subsequent instance of time, t , can be obtained from

$$\hat{\mathbf{n}} = R_z(-\Omega_s t) \hat{\mathbf{n}}_s = R_z(-\Omega_s t) \hat{\mathbf{n}}_0 \tag{17}$$

with $R_z(-\Omega_s t)$ the rotation matrix around the z -axis over an angle $-\Omega_s t$.

Due to, among others, the assumption of a constant sail attitude with respect to the Sun, the initial condition will not lead to a periodic orbit when integrated in the dynamics of Eq. (1). However, it can serve as a good initial guess for a differential corrector similar to the one described in Reference [36] for solar sail periodic orbits in the non-

autonomous solar sail Earth-Moon system. Note that this differential corrector includes a constraint to ensure that the period of the orbits equals $2\pi/\Omega_s$ in order for the orbital period and the period of the Sun around the binary system to be commensurable and thus for the orbits to be repeatable over time. The results are presented in Figure 10 to Figure 13, again for the assumption of a circular 1 AU heliocentric orbit. These figures show a variety of orbit families parameterized either by the solar sail cone angle, characteristic acceleration, the binary system's heliocentric orbit radius or mass distribution.

Starting with the results in Figure 10, these show a family of pole-sitter-like orbits for $a_0 = 10$ (see the penultimate column in Table 2 for corresponding sail performances) that are parameterized by the sail cone angle, $\alpha = \cos^{-1}(\hat{\mathbf{S}} \cdot \hat{\mathbf{n}}) = \tan^{-1}(n_z/n_x)$, see also Figure 9b. Figure 10a shows that the orbit can exist closer to the binary system's orbital plane for smaller cone angles (smaller out-of-plane components of the sail acceleration vector). However, for cone angles smaller than 73 deg, the differential corrector did not converge. Furthermore, the closer to the binary system (i.e., the smaller the cone angle), the more unstable the orbits become, see Figure 10b.

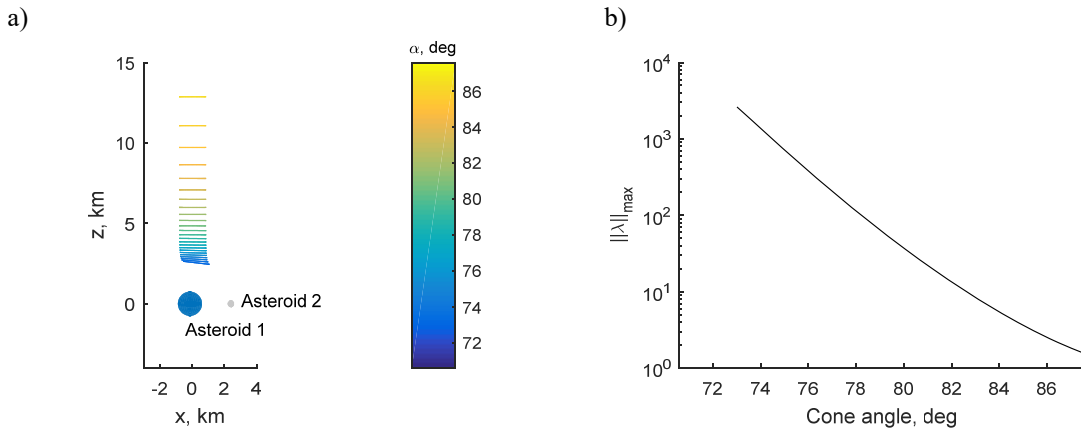


Figure 10 Family of pole-sitter-like orbits at 1999 KW4 for $a_0 = 10$, parameterized by the cone angle, α .
a) Orbits. b) Linear stability.

Instead of parameterizing by the cone angle, the orbits can also be parameterized by the required solar sail characteristic acceleration. For now, we assume a sail attitude equal to that of the orbit in Figure 10 at $z = 10$ km ($\alpha = 85.4$ deg). Such a large cone angle may not always fall within mission constraints [37], but is used here for illustrative purposes. Then, the family of orbits in Figure 11 can be obtained. Although the characteristic accelerations used to generate this family extend far beyond near-term sail technology, the figure shows that not

much can be gained from very high-performing solar sails: to halve the distance to the binary asteroid's orbital plane (e.g., from 10 km to 5 km) the characteristic acceleration needs to be increased by an order of magnitude.

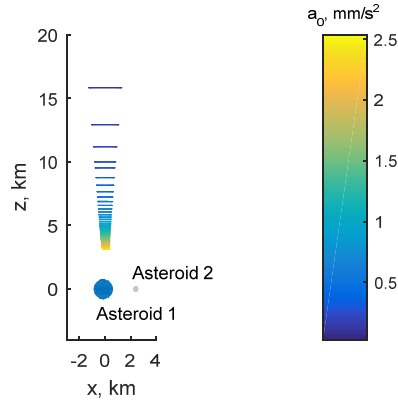


Figure 11 Family of pole-sitter-like orbits at 1999 KW4 for $\alpha = 85.4$ deg, parameterized by the characteristic acceleration, a_0 .

A third way of parameterization is shown in Figure 12, where families of periodic orbits for different heliocentric orbit radii of binary system 1999 KW4 are provided. Note that once again the sail attitude is fixed to $\alpha = 85.4$ deg and the sail performance is assumed to be $a_0 = 10$ at 1 AU. The figure shows that the pole-sitter-like orbits move farther away for larger heliocentric orbit radii, which is caused by the decrease in solar radiation pressure. An additional effect of an increased heliocentric orbit radius is a decrease in the orbit period because the Sun's synodic period decreases (Ω_s in Eq. (6) increases because n decreases) and approaches the binary system's rotational period. This effect is demonstrated in Figure 12b.

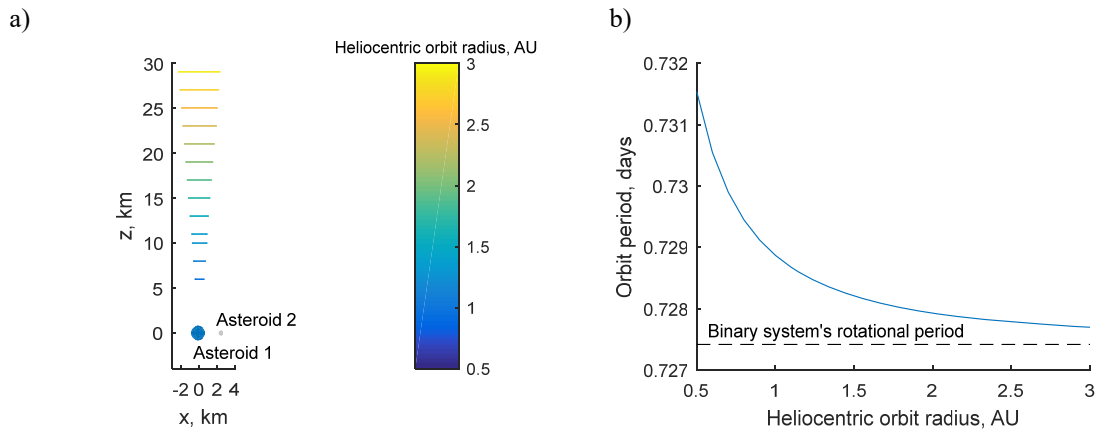


Figure 12 Family of pole-sitter-like orbits at 1999 KW4 for $a_0 = 10$ and $\alpha = 85.4$ deg, parameterized by the binary system's heliocentric orbit radius. a) Orbits. b) Orbital period.

Finally, in Figure 13 the effect of the mass distribution between the two asteroids is demonstrated. The figure shows a family of pole-sitter-like orbits for $a_0 = 10$, $\alpha = 85.4$ deg, and for a heliocentric orbit radius of 1 AU. While the mass distribution for binary system 1999 KW4 is set to $\nu = 0.9457$, Figure 13 shows the effect in case of errors in this value and takes it to the extreme where the mass distribution is inverted (‘Asteroid 2’ is more massive than ‘Asteroid 1’). For a clear presentation of the results, the reference frame is now centered at the *geometrical* center of the binary system. Furthermore, the sizes of the asteroids in Figure 13 are not accurate as these sizes will most likely change for different values for ν . However, what these results illustrate is how the orbit moves from hovering above ‘Asteroid 1’ (for $\nu > 0.5$) to hovering above ‘Asteroid 2’ (for $\nu < 0.5$).

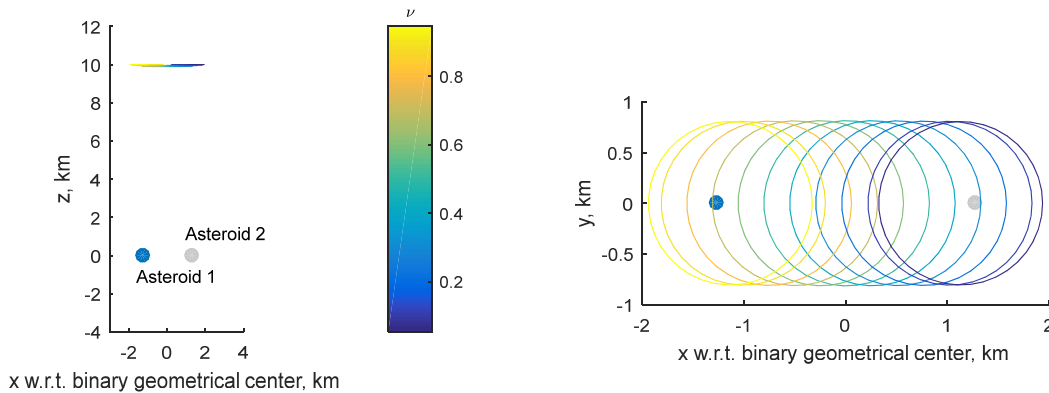


Figure 13 Family of pole-sitter-like orbits at 1999 KW4 for $a_0 = 10$ and $\alpha = 85.4$ deg, parameterized by the mass distribution between the two asteroids, ν .

VII. High-fidelity analyses

The results throughout Figure 10 to Figure 13 have shown that pole-sitter-like orbits exist for a range of sail attitudes and sail acceleration magnitudes and that the existence and shape of the pole-sitter-like orbits do not break down for heliocentric orbit radii or mass distributions different from those of binary system 1999 KW4. However, other system parameters have been neglected so far, including the eccentricity of the heliocentric orbit and the inclination of the orbit with respect to the binary system’s orbital plane. Because these perturbations act on a different time-scale than the period of the pole-sitter-like orbits, periodic orbits are not expected to exist under the effect of the heliocentric orbit eccentricity and inclination. Other effects, such as non-ideal properties of the solar sail and the non-spherical shape of one (or both) of the asteroids do not interfere with the orbital period and periodic

orbits may still be found. This section investigates the influence of each of these perturbations on the pole-sitter orbits of Section VI. Note that the pole-sitter orbits are selected for these high-fidelity analyses as they show some of the most unstable orbits, exist closest to the binary asteroid and use very large cone angles. The effects of the aforementioned perturbations are therefore expected to be largest and most relevant to these orbits.

A. Inclination of the heliocentric orbit

The results throughout this paper have so far assumed that the plane in which the two binary asteroids orbit each other and their heliocentric orbital plane are co-planar. However, from Table 3 it is clear that the actual inclination between those two planes is $i = 38.884$ degrees. This inclination will have a significant effect on the direction of sunlight, i.e., the unit vector $\hat{\mathbf{S}}$, which feeds into the solar sail acceleration vector, see Eq. (7), and the fourth body perturbation, see Eq. (3). Therefore, a more accurate definition for the unit vector $\hat{\mathbf{S}}$ in the bi-circular problem would be:

$$\hat{\mathbf{S}} = \begin{bmatrix} S_x & S_y & S_z \end{bmatrix}^T = R_z(-n_b t) R_y(i) R_z(\theta - \theta_0) \begin{bmatrix} 1 \\ 0 \\ 0 \end{bmatrix} = R_{tot} \begin{bmatrix} 1 \\ 0 \\ 0 \end{bmatrix}. \quad (18)$$

A supporting schematic is provided in Figure 14. Equation (18) assumes that at the start of the orbital analyses, at time $t = 0$ and when the binary system is at a certain true anomaly, θ_0 , in its heliocentric orbit, the projection of the sunlight-vector $\hat{\mathbf{S}}$ onto the (x, y) -plane points along the x -axis of the $R_2(\hat{\mathbf{x}}, \hat{\mathbf{y}}, \hat{\mathbf{z}})$ reference frame. Furthermore, at this time, the Sun is assumed to be above the Earth-Moon plane, see again Figure 14. Then, three rotations are applied: the first rotation, $R_z(\theta - \theta_0)$, around the z -axis over an angle $\theta - \theta_0$, accounts for the orbital motion of the binary system around the Sun; the second rotation, $R_y(i)$ accounts for the heliocentric orbit inclination; and the final rotation, $R_z(-n_b t)$ accounts for the rotation of the $\hat{\mathbf{S}}$ -vector due to the rotation of the binary asteroids around their barycenter. Note that, since the dynamics are integrated in time, the true anomaly, θ , in Eq. (18) is computed by numerically solving Kepler's equation at each integration step.

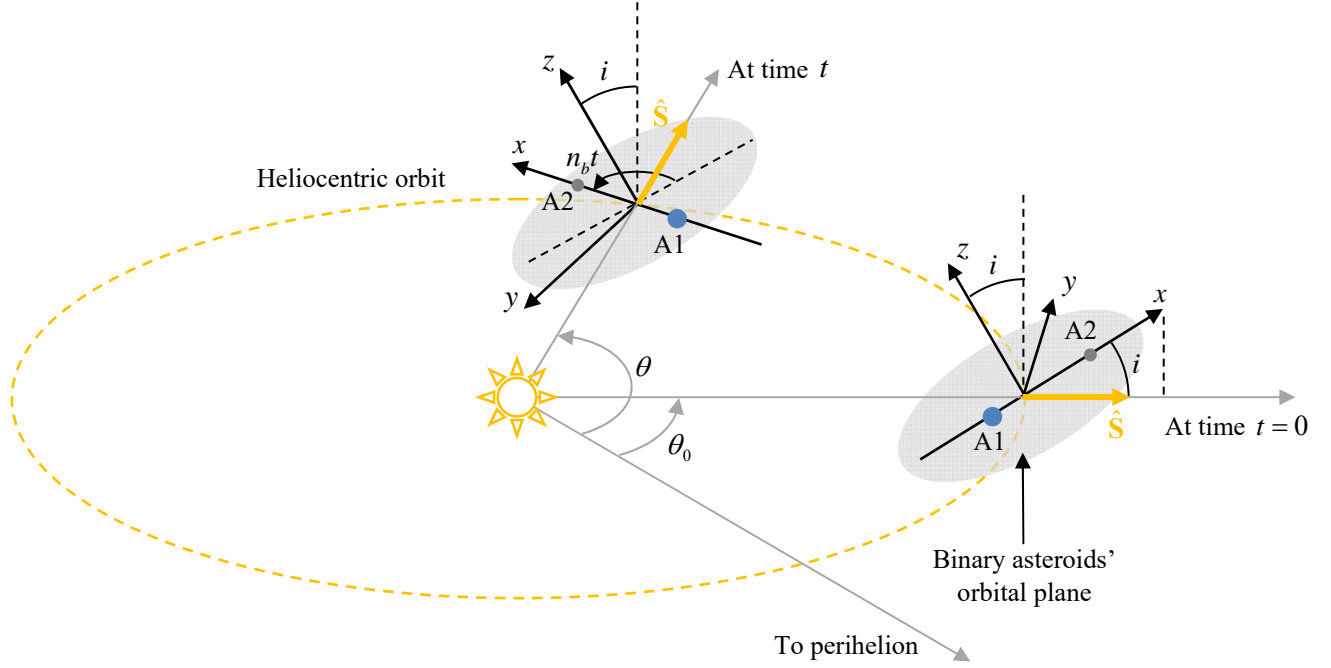


Figure 14 Schematic supporting the definition of the sunlight-vector, $\hat{\mathbf{S}}$, for an inclination between the binary asteroids' orbital plane and their heliocentric orbit.

B. Eccentricity of the heliocentric orbit

The next perturbation to account for is the eccentricity of the heliocentric orbit, $e = 0.688$ (see Table 3). This eccentricity causes a continuous change in the position vector of the Sun, \mathbf{r}_3 , which feeds into the fourth-body perturbation in Eq. (2) and can be defined as [38]:

$$\mathbf{r}_3 = -\frac{a(1-e^2)}{1+e\cos\theta}\hat{\mathbf{S}} \quad (19)$$

with $\hat{\mathbf{S}}$ from Eq. (18). The changing distance to the Sun also requires a continuous rescaling of the solar sail acceleration magnitude as the characteristic acceleration, a_0 , is defined *at a particular heliocentric distance*. The scaling factor to be used is $(r|_{a_0}/r_3)^2$ where $r|_{a_0}$ is the heliocentric distance used to define the value for a_0 .

C. Non-ideal sail properties

In the analyses up to this point, an ideal solar sail reflectance model has been assumed, which considers the sail to be a perfect mirror, resulting in a solar sail induced acceleration vector that acts perpendicular to the solar sail membrane, along the sail normal, $\hat{\mathbf{n}}$. However, in reality, the sail will not be a perfect mirror and, as a result, the

acceleration vector will include a component tangential to the sail, $\hat{\mathbf{t}}$, resulting in an acceleration vector acting in the direction $\hat{\mathbf{m}}$, see Figure 15:

$$\mathbf{a}_s = a_n \hat{\mathbf{n}} + a_t \hat{\mathbf{t}} = a_s \hat{\mathbf{m}}. \quad (20)$$

By including absorption, specular and diffuse reflection, and thermal emission in the reflectance model (referred to as the “optical sail reflectance model”), the magnitude of the solar sail acceleration components along these normal and tangential directions are given by [3]:

$$\begin{aligned} a_n &= \frac{1}{2} a_0 \left[(1 + \tilde{r}s) \cos^2 \alpha + B_f (1 - s) \tilde{r} \cos \alpha + (1 - \tilde{r}) \frac{\varepsilon_f B_f - \varepsilon_b B_b}{\varepsilon_f + \varepsilon_b} \cos \alpha \right] \\ a_t &= \frac{1}{2} a_0 (1 - \tilde{r}s) \cos \alpha \sin \alpha \end{aligned} \quad (21)$$

In Eqs. (20) and (21), $\tilde{r} = 0.91$ is the reflectivity coefficient that indicates the fraction of reflected photons, $s = 0.94$ indicates the fraction of photons that are *specularly* reflected, while the term $(1 - s)$ indicates the fraction of photons that are *diffusely* reflected; $B_f = 0.79$ and $B_b = 0.67$ are the non-Lambertian coefficients of the front (subscript ‘ f ’) and back (subscript ‘ b ’) of the sail, and $\varepsilon_f = 0.025$ and $\varepsilon_b = 0.27$ are the emissivity coefficients of the front and back of the sail, respectively. The values for these optical coefficients have recently been obtained for NASA’s proposed Near Earth Asteroid (NEA) Scout mission [37].

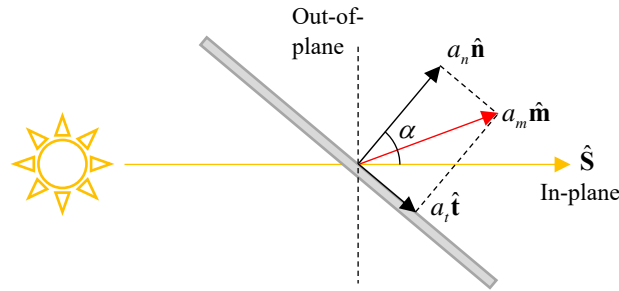


Figure 15 Side-view schematic of non-ideal solar sail acceleration components.

Continuing the assumption for the pole-sitter orbits of a fixed attitude of the sail with respect to the direction of sunlight, see Figure 15, the normal and tangential unit vectors with respect to the sunlight-direction (subscript ‘ S ’) can be defined as:

$$\hat{\mathbf{n}}_s = \begin{bmatrix} \cos \alpha \\ 0 \\ \sin \alpha \end{bmatrix}, \quad \hat{\mathbf{t}}_s = \begin{bmatrix} \sin \alpha \\ 0 \\ -\cos \alpha \end{bmatrix}. \quad (22)$$

However, for use in the dynamics, the acceleration needs to be defined in the $R_2(\hat{\mathbf{x}}, \hat{\mathbf{y}}, \hat{\mathbf{z}})$ -frame, which is achieved through:

$$\mathbf{a}_s = R_{tot} \left(a_n \hat{\mathbf{n}}_s + a_t \hat{\mathbf{t}}_s \right) \quad (23)$$

with R_{tot} defined in Eq. (18).

D. Oblateness of the binary asteroids

The final perturbation accounted for is the fact that the two asteroids of binary system 1999 KW4 do not satisfy the assumption of spherically shaped bodies. In particular, Table 3 shows a significant difference between the bodies' equatorial and polar radii, the effect of which can be included in the dynamics through the following perturbing potential for the oblateness of the two asteroids [39, 40]:

$$U_{J_2} = \frac{(1-\mu)A_1}{2r_1^3} \left(1 - \frac{3z^2}{r_1^2} \right) + \frac{\mu A_2}{2r_2^3} \left(1 - \frac{3z^2}{r_2^2} \right). \quad (24)$$

The gradient of this potential can then be added to the right hand side of Eq. (1). In Eq. (24), A_1 and A_2 are the oblateness coefficients, defined as:

$$A_j = \frac{R_j^2 - R_{j,p}^2}{5\kappa^2} \quad j = 1, 2, \quad (25)$$

where R_j and $R_{j,p}$ are the equatorial and polar radii of the two asteroids and κ the previously defined distance between the two asteroids (see Table 3). Finally, the oblateness of the bodies also causes a change in the mean motion of the binary system, i.e., in the angular velocity of the $R_2(\hat{\mathbf{x}}, \hat{\mathbf{y}}, \hat{\mathbf{z}})$ -frame [39]:

$$\Omega_{J_2} = \sqrt{1 + \frac{3}{2}(A_1 + A_2)}. \quad (26)$$

E. High-fidelity dynamical system

Combining all information of Sections VII.A to VII.D results in the following high-fidelity dynamical system defined in the $R_2(\hat{\mathbf{x}}, \hat{\mathbf{y}}, \hat{\mathbf{z}})$ -frame:

$$\ddot{\mathbf{r}} + 2\boldsymbol{\Omega} \times \dot{\mathbf{r}} = \nabla U + \mathbf{a}_s \quad (27)$$

with

$$U = \left(\frac{1-\mu}{r_1} + \frac{\mu}{r_2} \right) + \frac{\Omega_{J_2}^2}{2} (x^2 + y^2) + \mu_3 \left(\frac{1}{r_4} - \frac{\mathbf{r} \cdot \mathbf{r}_3}{r_3^3} \right) + \frac{(1-\mu)A_1}{2r_1^3} \left(1 - \frac{3z^2}{r_1^2} \right) + \frac{\mu A_2}{2r_2^3} \left(1 - \frac{3z^2}{r_2^2} \right). \quad (28)$$

In Eqs. (27) and (28), the variables μ , μ_3 , \mathbf{r} , \mathbf{r}_1 , \mathbf{r}_2 and \mathbf{r}_4 are as defined in Section II, while all other variables need to be redefined according to the information provided in Sections VII.A to VII.D: \mathbf{r}_3 in Eq. (19), $\hat{\mathbf{S}}$ in Eq. (18), \mathbf{a}_s in Eqs. (21)-(23), and Ω_{J_2} , A_1 , and A_2 in Eqs. (25)-(26).

F. Results for single pole-sitter-like orbit revolution

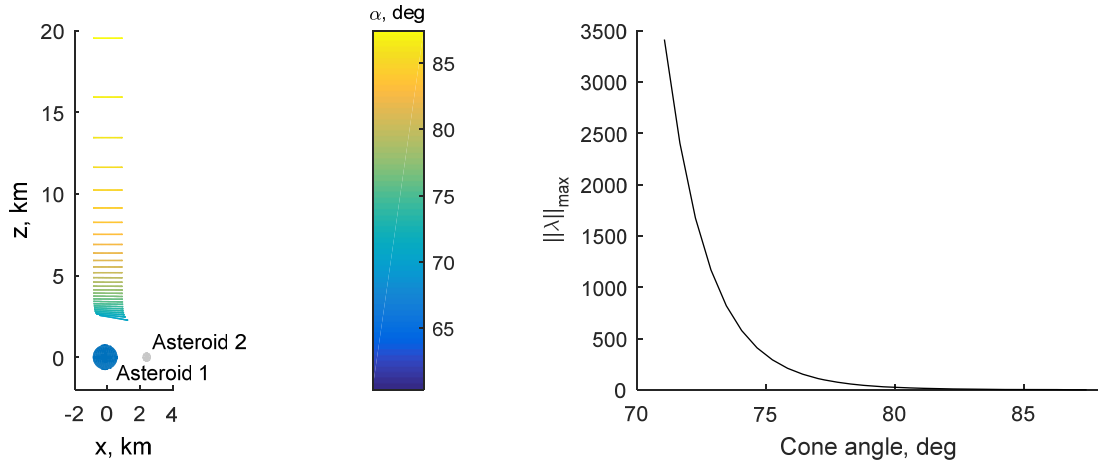
When considering the effect of the perturbations on a *single* pole-sitter-like orbit revolution, some assumptions can be made that allow the periodicity of the dynamics to be preserved such that periodic pole-sitter-like orbits can still be obtained even under the effect of the perturbations and that the differential correction scheme of Section IV can still be applied. In particular, because the orbit period of the pole-sitter is much smaller than the period of the heliocentric orbit, the out-of-plane component of the unit vector $\hat{\mathbf{S}}$ and the heliocentric orbit radius, r_3 , can be assumed constant, removing the non-periodicity that these two elements introduce over longer periods of time.

We furthermore consider two specific configurations: one where the binary system is at perihelion at time $t = 0$ ($\theta_0 = 0$ in Figure 14) and one where the binary system is at aphelion at time $t = 0$ ($\theta_0 = \pi$). Combining these configurations with the previous assumption that the Sun is at its most out-of-plane location at the initial time, provides a conservative approach as from the Keplerian elements of 1999 KW4 (see Table 3) it is clear that the Sun is almost in the plane of the binary system at perihelion and aphelion.

Changing from a 1 AU circular heliocentric orbit as used throughout Section IV to the conditions at aphelion and perihelion (but neglecting all other perturbations for now), results in the orbit families appearing in Figure 16. At aphelion, the heliocentric orbit radius is very close to 1 AU (1.084 AU), resulting in an orbit family very similar to the one found in Figure 10. However, the heliocentric orbital speed at aphelion is much smaller than in the previously assumed 1 AU circular orbit, resulting in a larger value for Ω_s (see Table 3) and thus a slightly shorter pole-sitter-like orbit period. At perihelion, where the solar sail acceleration magnitude is a factor 25 larger than at 1 AU, pole-sitter-like orbits only exist for very large cone angles. As mentioned previously, such large cone angles often do not fall within mission constraints [37]. Therefore, the analyses on the effect of the perturbations will focus

on the orbit family at aphelion and in particular on the orbit with the smallest cone angle of $\alpha = 71.1$ deg that also exhibits the largest linear instability.

a)



b)

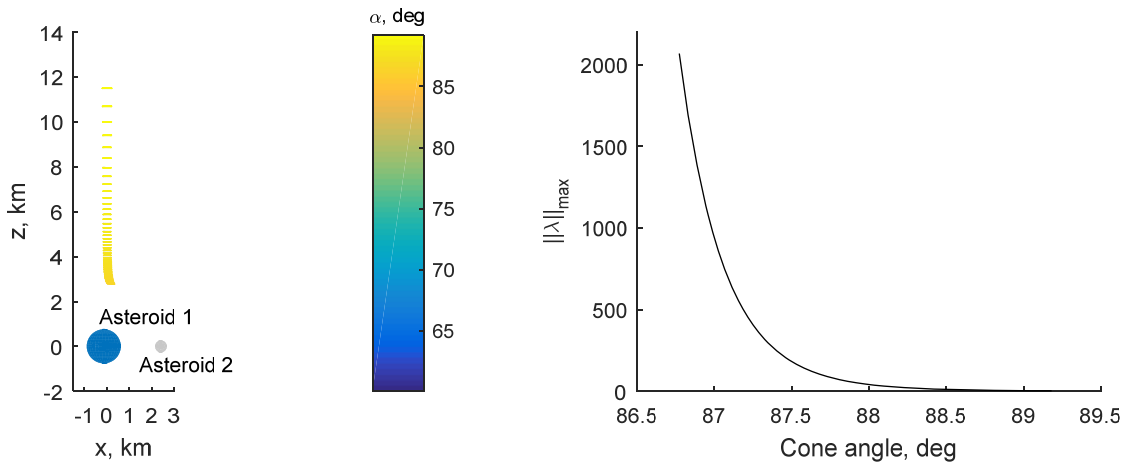
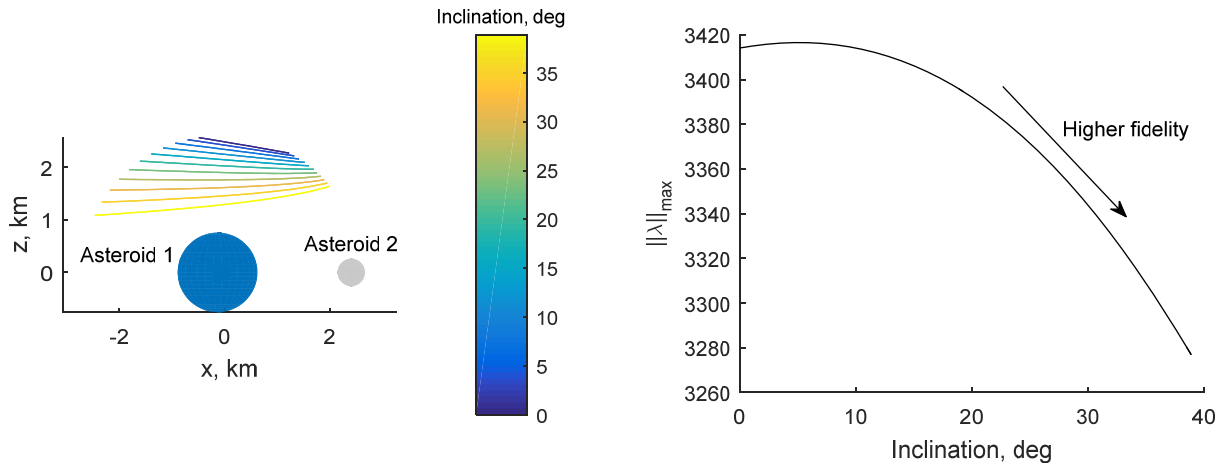


Figure 16 Family of pole-sitter-like orbits and their stability parameterized by the cone angle, α .

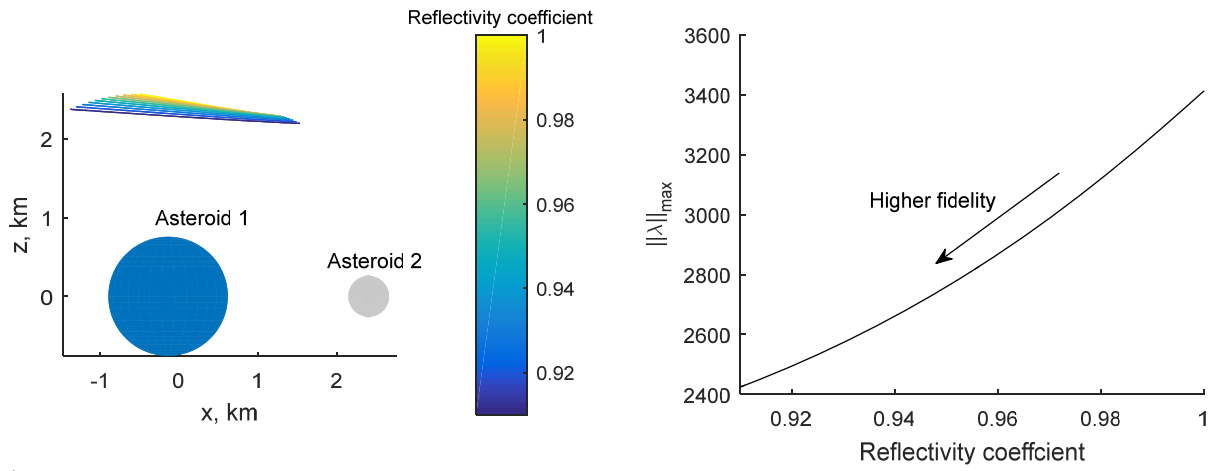
a) At aphelion. b) At perihelion.

The results for each of the remaining perturbations separately, as well as the effect of all perturbations combined, appear in Figure 17. To ensure convergence of the differential corrector scheme, each perturbation is introduced gradually through a continuation scheme similar to the one explained in Section V and the intermediate results are presented through the color schemes in Figure 17. The figure shows that each of the perturbations drives the pole-sitter-like orbits towards Asteroid 1 with the largest impact from the heliocentric orbit inclination and the smallest effect from the oblateness of the asteroids. Finally, and interestingly, each perturbation has a stabilizing effect on the orbits.

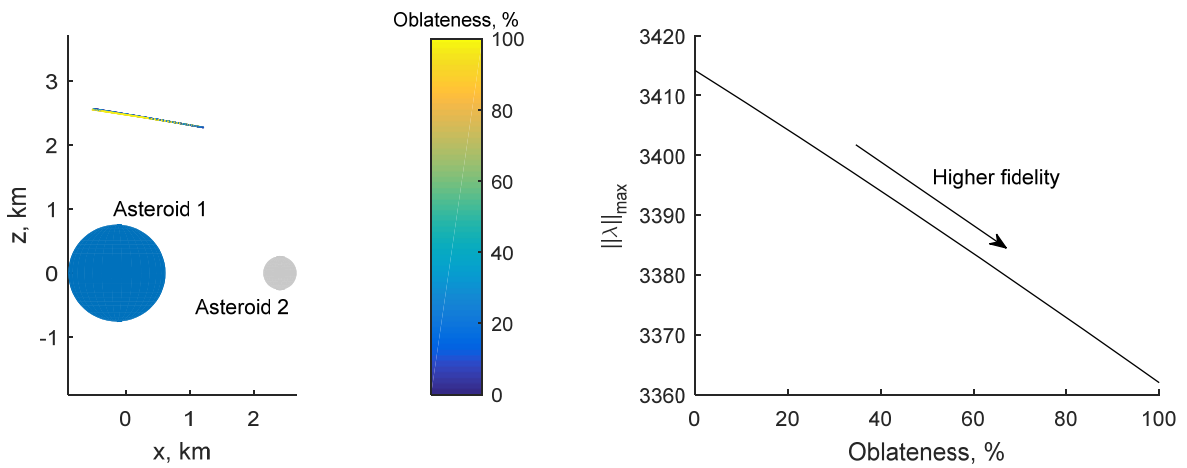
a)



b)



c)



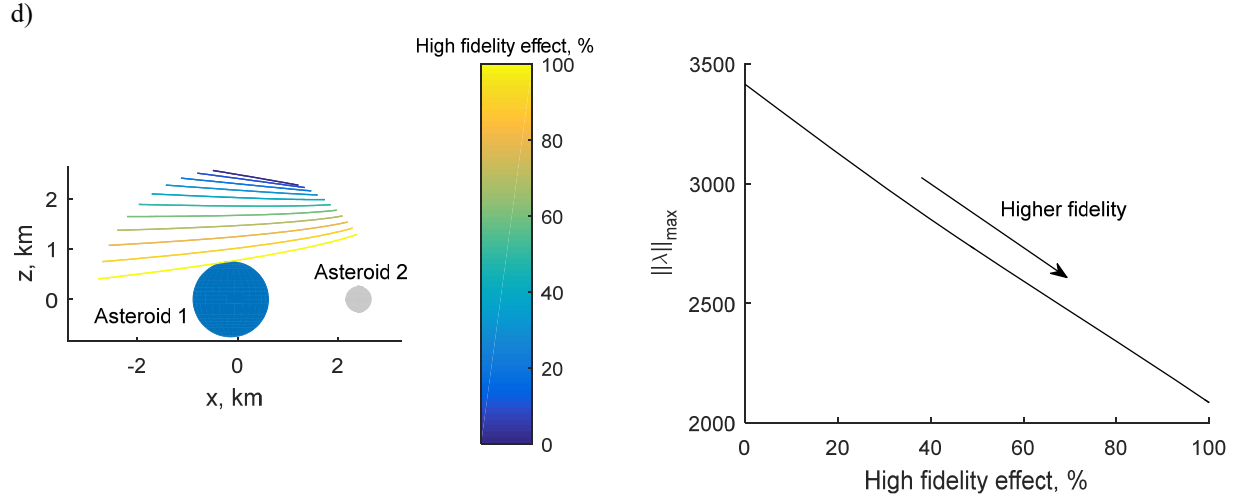


Figure 17 Effect of high-fidelity effects on one pole-sitter-like orbit revolution at aphelion with $\alpha = 71.1$ deg. a) Inclination of heliocentric orbit. b) Non-ideal solar sail. c) Oblateness. d) All perturbations combined.

G. Results for multiple pole-sitter-like orbit revolutions

While the results in the previous section only considered the higher-fidelity effects over a single pole-sitter-like orbit revolution and assumed a constant out-of-plane component of the unit vector $\hat{\mathbf{S}}$ and a constant heliocentric orbit radius, this section extends the analyses to multiple pole-sitter orbit periods. Then, the variations in the out-of-plane component of $\hat{\mathbf{S}}$ and the changing heliocentric orbit radius due to the eccentricity can no longer be neglected and need to be accounted for. To once again stay as close as possible to the unperturbed orbit, the same multiple shooting differential algorithm as outlined in Section V is applied, using a continuation scheme to slowly introduce the perturbations starting from the unperturbed orbit. The result for 20 orbit revolutions (spanning 14.5 days) appears in Figure 18a and shows a trajectory that is very close to the single-revolution, fully perturbed orbit of Figure 17d. The distance over time between these single- and multi-revolution trajectories appears in Figure 18 and provides a measure for the effect of the changing out-of-plane component of the unit vector $\hat{\mathbf{S}}$ and heliocentric orbit radius around aphelion.

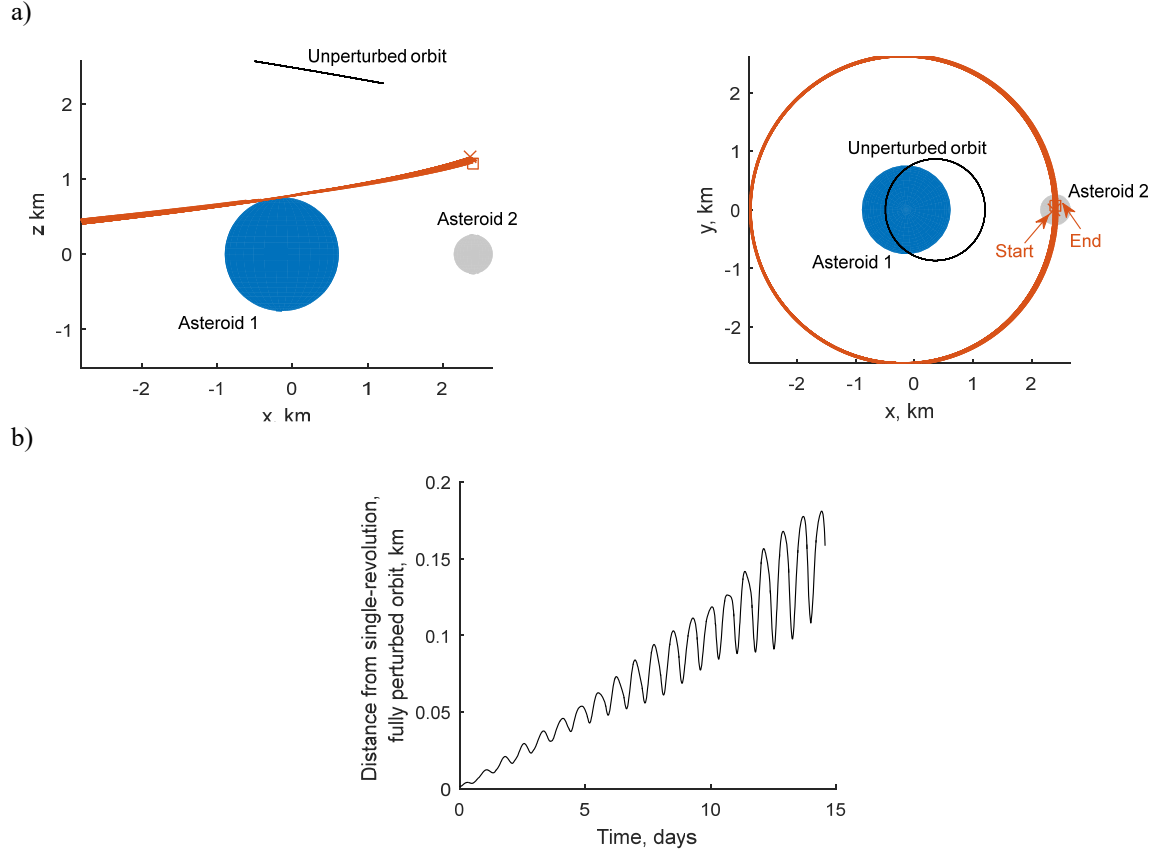


Figure 18 Effect of high-fidelity effects over 20 orbit revolutions of the pole-sitter-like orbit starting at aphelion with $\alpha = 71.1$ deg. a) Orbit. b) Distance from orbit in Figure 17d.

VIII. Conclusions

This paper has demonstrated the existence of solar sail artificial equilibrium points (AEPs) at asteroids and binary systems as well as solar sail periodic orbits above their orbital planes. For the single asteroid case, solar sail acceleration contours have been obtained in the Hill + SRP problem that allow the sailcraft to remain stationary with respect to the asteroid on either the Sun-lit or dark side of the asteroid and either in or above its orbital plane. Furthermore, families of solar sail periodic orbits around these AEPs have been generated, where each orbit within a family only differs in its out-of-plane amplitude. These orbits have been found for near-term sail technology and for periods equal to a significant fraction of the asteroid's heliocentric orbital period. When taking asteroid Vesta as a test case, sailcraft-asteroid distances in the order of 10^4 km can be achieved. When adding a fourth body to the Hill + SRP dynamics to simulate a binary system, the smaller asteroid creates a small oscillatory motion around the

displaced orbits, causing non-periodic motion. When modelling the binary system in the bi-circular + SRP problem, AEPs and truly periodic solar sail orbits can be obtained, though the required sail attitude and characteristic acceleration to maintain a particular AEPs become time-dependent due to the changing direction of sunlight. Taking binary system 1999 KW4 as a test case, families of pole-sitter-like orbits above the binary orbital plane have been generated that can be parameterized, for example, by the required sail characteristic acceleration, the sail attitude, the heliocentric distance or even the mass distribution within the binary system. For large ranges in the values for these parameters, the existence of pole-sitter-like orbits above the binary system has been demonstrated at sailcraft-binary distances in the order of 10 km for near-term sail technology. While all orbits presented (both for the single asteroid case and the binary system) are linearly unstable, they do allow a unique vantage point from where to observe the asteroid or asteroid pair. Furthermore, all orbits exist for a simple solar sail steering law where the attitude is fixed with respect to the Sun, which greatly simplifies mission operations. Finally, for the most interesting and unstable orbits, the pole-sitter-like orbits, the effect of higher fidelity effects have been investigated, including the 38.884 deg inclination of the binary system orbital plane with respect to its heliocentric orbit, the eccentricity of the heliocentric orbit, non-ideal properties of the solar sail and the oblateness of both binary asteroids. The net result is a shift of the pole-sitter-like orbits towards the binary asteroids. As these effects all act on different time scales, often not commensurable with the period of the pole-sitter-like orbits, non-periodic motion results, but through the use of a multiple shooting differential correction, the trajectory can be shown to maintain a pole-sitter-like shape for 15 days starting from the binary system's aphelion.

Acknowledgments

Jeannette Heiligers would like to acknowledge support from the Marie Skłodowska-Curie Individual Fellowship 658645 - S4ILS: Solar Sailing for Space Situational Awareness in the Lunar System.

References

1. Tsuda, Y., Mori, O., Funase, R., Sawada, H., Yamamoto, T., Saiki, T., Endo, T., Yonekura, K., Hoshino, H., and Kawahuchi, J., "Achievement of IKAROS - Japanese deep space solar sail demonstration mission," *Acta Astronautica*; Vol. 82, 2013, pp. 183-188. doi: 10.1016/j.actaastro.2012.03.032
2. Johnson, L., Whorton, M., Heaton, A., Pinson, R., Laue, G., and Adams, C., "NanoSail-D: A Solar Sail Demonstration Mission," *Acta Astronautica*; Vol. 68, 2011, pp. 571-575. doi: 10.1016/j.actaastro.2010.02.008
3. McInnes, C.R., "Solar Sailing: Technology, Dynamics and Mission Applications," *Springer-Praxis Books in Astronautical Engineering*, Springer-Verlag, Berlin, 1999.

4. Vulpetti, G., Johnson, L., and Matloff, G.L., "Solar Sails A Novel Approach to Interplanetary Travel, 2nd Edition," *Springer-Praxis Books in Space Exploration*, 2nd ed., Springer Science+Business Media, New York, 2015.
5. Macdonald, M., McInnes, C., Alexander, D., and Sandman, A., "GeoSail: Exploring the Magnetosphere Using a Low-cost Solar Sail," *Acta Astronautica*; Vol. 59, 2006, pp. 757-767. doi: 10.1016/j.actaastro.2005.07.023
6. Macdonald, M. and McInnes, C., "Solar Sail Science Mission Applications and Advancement," *Advances in Space Research*; Vol. 48, No. 11, 2011, pp. 1702-1716. doi: 10.1016/j.asr.2011.03.018
7. McInnes, C.R., Macdonald, M., Angelopolous, V., and Alexander, D., "GEOSAIL: Exploring the Geomagnetic Tail Using a Small Solar Sail," *Journal of Spacecraft and Rockets*; Vol. 38, No. 4, 2001, pp. 622-629. doi: 10.2514/2.3727
8. Macdonald, M., Hughes, G., McInnes, C., A, L., Falkner, P., and Atzei, A., "GeoSail: An Elegant Solar Sail Demonstration Mission," *Journal of Spacecraft and Rockets*; Vol. 44, No. 4, 2007, pp. 784-796. doi: 10.2514/1.22867
9. West, J.L., "The GeoStorm Warning Mission: Enhanced Opportunities Based on New Technology," *14th AAS/AIAA Spaceflight Mechanics Conference*, AAS-04-102, Maui, Hawaii, 2004.
10. Heiligers, J., Diedrich, B., Derbes, B., and McInnes, C.R., "Sunjammer: Preliminary End-to-End Mission Design," *2014 AIAA/AAS Astrodynamics Specialist Conference*, San Diego, CA, USA, 2014.
11. Dachwald, B., Boehnhardt, H., Broj, U., Geppert, U.R.M.E., Grundmann, J.-T., Seboldt, W., Seefeldt, P., Spietz, P., Johnson, L., Kühr, E., Mottola, S., Macdonald, M., McInnes, C.R., Vasile, M., and Reinhard, R., *Gossamer Roadmap Technology Reference Study for a Multiple NEO Rendezvous Mission*, in *Advances in Solar Sailing*, M. Macdonald, Editor. 2014, Springer Berlin Heidelberg: Berlin, Heidelberg. p. 211-226.
12. Peloni, A., Ceriotti, M., and Dachwald, B., "Solar-Sail Trajectory Design for a Multiple Near-Earth-Asteroid Rendezvous Mission," *Journal of Guidance, Control, and Dynamics*; Vol., 2016, pp. 0-0. doi: 10.2514/1.G000470
13. McNutt, L., Johnson, L., Clardy, D., Castillo-Rogez, J., Frick, A., and Jones, L., "Near-Earth Asteroid Scout," *AIAA SPACE 2014 Conference and Exposition*, American Institute of Aeronautics and Astronautics, San Diego, CA, 2014.
14. Scheeres, D.J., "Orbital Motion in Strongly Perturbed Environments - Applications to Asteroid, Comet and Planetary Satellite Orbiters," *Springer-Praxis Books in Astronautical Engineering*, Berlin Heidelberg, 2012.
15. Scheeres, D.J., "Orbit Mechanics About Asteroids and Comets," *Journal of Guidance, Control, and Dynamics*; Vol. 35, No. 3, 2012, pp. 987-997. doi: 10.2514/1.57247
16. Morrow, E., Scheeres, D.J., and Lubin, D., "Solar Sail Operations at Asteroids," *Journal of Spacecraft and Rockets*; Vol. 38, No. 2, 2001, pp. 279-286. doi: 10.2514/2.3682
17. Gong, S. and Li, J., "Equilibria near Asteroids for Solar Sails with Reflection Control Devices," *Astrophysics and Space Science*; Vol. 355:0, 2015. doi: 10.1007/s10509-014-2165-7
18. Williams, T. and Abate, M., "Capabilities of Furlable Solar Sails for Asteroid Proximity Operations," *Journal of Spacecraft and Rockets*; Vol. 46, No. 5, 2009, pp. 967-975. doi: 10.2514/1.30355
19. Zeng, X., Gong, S., Li, J., and Alfriend, K.T., "Solar Sail Body-Fixed Hovering over Elongated Asteroids," *Journal of Guidance, Control, and Dynamics*; Vol. 39, No. 6, 2016, pp. 1223-1231. doi: 10.2514/1.G001061
20. Zeng, X.-Y., Jiang, F.-H., and Li, J.-F., "Asteroid Body-Fixed Hovering Using Nonideal Solar Sails," *Research in Astronomy and Astrophysics*; Vol. 15, No. 4, 2015, pp. 597-607. doi: 10.1088/1674-4527/15/4/011
21. McKay, R.J., Macdonald, M., Biggs, J., and McInnes, C., "Survey of Highly Non-Keplerian Orbits with Low-Thrust Propulsion," *Journal of Guidance, Control, and Dynamics*; Vol. 34, No. 3, 2011. doi: 10.2514/1.52133
22. Morimoto, M., Yamakawa, H., and Uesugi, K., "Periodic Orbits with Low-Thrust Propulsion in the Restricted Three-Body Problem," *Journal of Guidance, Control, and Dynamics*; Vol. 29, No. 5, 2006, pp. 1131-1139. doi: 10.2514/1.19079
23. Bidy, C. and Svitek, T., "LightSail-1 Solar Sail Design and Qualification," *Proceedings of the 41st Aerospace Mechanisms Symposium*, Pasadena, CA, 2012.
24. Bellerose, J. and Scheeres, D., "Restricted Full Three-Body Problem: Application to Binary System 1999 KW4," *Journal of Guidance, Control, and Dynamics*; Vol. 31, No. 1, 2008, pp. 162-171. doi: 10.2514/1.30937
25. Scheeres, D.J., Fahnestock, E.G., Ostro, S.J., Margot, J.-L., Benner, L.A.M., Broschart, S.B., Bellerose, J., Giorgini, J.D., Nolan, M.C., Magri, C., Pravec, P., Scheirich, P., Rose, R., Jurgens, R.F., De Jong, E.M., and Suzuki, S., "Dynamical Configuration of Binary Near-Earth Asteroid (66391) 1999 KW4," *Science*; Vol. 314, No. 5803, 2006, pp. 1280-1283. doi: 10.1126/science.1133599
26. Ostro, S.J., Margot, J.-L., Benner, L.A.M., Giorgini, J.D., Scheeres, D.J., Fahnestock, E.G., Broschart, S.B., Bellerose, J., Nolan, M.C., Magri, C., Pravec, P., Scheirich, P., Rose, R., Jurgens, R.F., De Jong, E.M., and Suzuki, S., "Radar Imaging of Binary Near-Earth Asteroid (66391) 1999 KW4," *Science*; Vol. 314, No. 5803, 2006, pp. 1276-1280. doi: 10.1126/science.1133622
27. Baoyin, H. and McInnes, C., "Solar Sail Halo Orbits at the Sun-Earth Artificial L1-point," *Celestial Mechanics and Dynamical Astronomy*; Vol. 94, 2006, pp. 155-171. doi: 10.1007/s10569-005-4626-3
28. Waters, T.J. and McInnes, C.R., "Periodic Orbits Above the Ecliptic in the Solar-Sail Restricted Three-Body Problem," *Journal of Guidance, Control, and Dynamics*; Vol. 30, No. 3, 2007, pp. 687-693. doi: 10.2514/1.26232
29. Howell, K.C., "Three-Dimensional, Periodic, 'Halo' Orbits," *Celestial Mechanics and Dynamical Astronomy*; Vol. 32, 1983, pp. 53-71. doi: 10.1007/BF01358403
30. Parker, J.S. and Anderson, R.L., "Low-Energy Lunar Trajectory Design," *Deep Space Communications and Navigation Series*, Jet Propulsion Laboratory, Pasadena, California, USA, 2013.

31. Howell, K.C. and Pernicka, H.J., "Numerical Determination of Lissajous Trajectories in the Restricted Three-Body Problem," *Celestial Mechanics*; Vol. 41, 1988, pp. 107-124
32. Marchand, B.G., Howell, K.C., and Wilson, R.S., "Improved Corrections Process for Constrained Trajectory Design in the n-Body Problem," *Journal of Spacecraft and Rockets*; Vol. 44, No. 4, 2007, pp. 884-897
33. Heiligers, J., Ceriotti, M., McInnes, C.R., and Biggs, J.D., "Mission Analysis and Systems Design of a Near-Term and Far-Term Pole-Sitter Mission," *Acta Astronautica*; Vol. 94, No. 1, 2014. doi: 10.1016/j.actaastro.2012.12.015
34. Ceriotti, M., Heiligers, J., and McInnes, C.R., "Trajectory and Spacecraft Design for a Pole-Sitter Mission," *Journal of Spacecraft and Rockets*; Vol. 51, No. 1, 2014, pp. 311-326. doi: 10.2514/1.A32477
35. Walmsley, M., Heiligers, J., Ceriotti, M., and McInnes, C., "Optimal Trajectories for Planetary Pole-Sitter Missions," *Journal of Guidance, Control, and Dynamics, Under Review*; Vol., 2016
36. Heiligers, J., Macdonald, M., and Parker, J.S., "Extension of Earth-Moon Libration Point Orbits with Solar Sail Propulsion," *Astrophysics and Space Sciences, In Press*; Vol. 361 : 241, 2016. doi: 10.1007/s10509-016-2783-3
37. Heaton, A., Ahmad, N., and Miller, K., "Near Earth Asteroid Scout Solar Sail Thrust and Torque Model," *4th International Symposium on Solar Sailing*, Kyoto, Japan, 2017.
38. Wertz, J.R., "Mission Geometry; Orbit and Constellation Design and Management," Space Technology Library, Microcosm Press/Kluwer Academic Publishers, El Segundo, USA/London, UK, 2001.
39. Sharma, R.K. and Subba Rao, P.V., "Stationary solutions and their characteristic exponents in the restricted three-body problem when the more massive primary is an oblate spheroid," *Celestial mechanics*; Vol. 13, No. 2, 1976, pp. 137-149. doi: 10.1007/bf01232721
40. Zeng, X.-Y., Liu, X.-D., and Li, J.-F., "Extension of the Rotating Dipole Model with Oblateness of Both Primaries," *Research in Astronomy and Astrophysics*; Vol. 17, No. 1, 2017. doi: 10.1088/1674-4527/17/1/2